*Korean J. Chem. Eng.*, 40(6), 1401-1417 (2023)
DOI: 10.1007/s11814-022-1332-8

pISSN: 0256-1115
eISSN: 1975-7220

# Synergistic and sustainable activation of peroxymonosulfate by nanoscale MWCNTs-$CuFe_2O_4$ as a magnetic heterogeneous catalyst for the efficient removal of levofloxacin

**Jing Zhao and Pengfei Xiao†**

College of Forestry, Northeast Forestry University, Harbin 150040, China
(*Received 11 August 2022 • Revised 4 October 2022 • Accepted 1 November 2022*)

**Abstract**−Nanoscale $CuFe_2O_4$ was anchored on the surface of multiwalled carbon nanotubes (MWCNTs) as a magnetic heterogeneous catalyst to achieve efficient and sustainable activation of peroxymonosulfate and degradation of levofloxacin through the synergistic effect of the above materials. The catalyst properties were characterized by a series of detection techniques. It was found that the mass ratio of MWCNTs-$CuFe_2O_4$, operational parameters and common interfering substances influenced the levofloxacin removal efficiency to a certain extent. This study sheds light on the ultraefficient removal of levofloxacin with the MWCNTs-$CuFe_2O_4$(1 : 3)/peroxymonosulfate system, which has advantages over other reaction systems. More importantly, we propose two pathways of peroxymonosulfate activation, including free radicals and nonfree radicals, in which superoxide radicals and signal oxygen are the main active species. In addition, we observed that the MWCNT surface groups contributed to the peroxymonosulfate activation processes with the generation of extra reactive species. The $Fe^{3+}/Fe^{2+}$ and $Cu^{2+}/Cu^{+}$ redox cycles are conducive to the continuous generation of active species. The results of the catalyst recycling test, metal ion leaching test and mineralization test suggested that the fabricated catalyst had excellent catalytic stability, sustainability and mineralization ability. In addition, twenty-one intermediates were detected using liquid chromatography-mass spectrometry, and three possible degradation pathways were further proposed. MWCNTs-$CuFe_2O_4$ makes up for the shortcomings of transition metals and single carbon materials in activating peroxymonosulfate to treat wastewater and have significant potential to improve the separation and catalytic capacity of the catalyst. This study provides new ideas for the design of high-performance multiphase catalysts for applications in catalytic oxidation and proposes new insights into the mechanistic investigation.

Keywords: Heterogeneous Catalysis, Nanoscaled Magnetic Catalyst, Activated Peroxymonosulfate, Levofloxacin Degradation, Synergistic Effect, Reactive Mechanisms

## INTRODUCTION

Recently, pharmaceuticals and personal care products (PPCPs) have aroused increasing awareness due to their extensive applications in human and veterinary medicine, leading to frequent detection in various bodies of water [1,2]. In particular, antibiotics, as a large class of typical PPCPs, have the characteristics of toxicity, limited metabolism and durable pharmacological activity, which results in more than 30% of consumed antibiotics being discharged into the aqueous environment and further seriously threatening the ecosystem and human health [3]. Among them, levofloxacin (LEV), as the most consumed antibiotic, is a third-generation fluoroquinolone (FQ) antibiotic with a core quinolone ring structure containing a fluorine atom and a broader spectrum of activity against gram-positive and gram-negative bacteria. In this sense, the development of an effective method for removing LEV has become increasingly urgent [4,5].

Recently, advanced oxidation process (AOP)-based sulfate radicals ($SO_4^{\bullet-}$) have garnered increasing attention as an emerging and effective technology for removing numerous antibiotic pollutants from wastewater due to the unique advantages of $SO_4^{\bullet-}$ including the higher standard redox potential ($E_0$=2.5-3.1 V), longer half-life ($t_{1/2}$=30-40 μs), higher selectivity and low self-quenching effect [6,7]. The processes can be performed conveniently by the activation of peroxymonosulfate (PMS, $HSO_5^-$) or peroxydisulfate (PDS, $S_2O_8^{2-}$) via various methods, such as heat, ultrasound, irradiation sources, transition metal cations, and carbon catalysts [8-10]. Among them, spinel ferrites, with a general formula of $MFe_2O_4$ (M=Co, Cu, Ni, Mn, etc.), have been widely used for PMS activation to generate a large amount of $SO_4^{\bullet-}$ [11,12]. In particular, $CuFe_2O_4$ exhibits superior catalytic activity due to easy separation and recyclability based on high saturation magnetization, excellent electronic properties, low electrical resistivity and low toxicity in comparison with other ferrites [13]. Nevertheless, the properties of $CuFe_2O_4$ lead to particle agglomeration, which hinders catalytic reactions due to the nonuniform population of active sites and constrains the electron transfer rate [14].

To overcome these defects, some researchers have proposed that metal oxides can be immobilized on porous supporting materials, such as graphene, zeolite, kaolin and nickel foam [9]. Compared to the supporting materials mentioned above, multiwalled carbon nanotubes (MWCNTs) with a one-dimensional nanotube struc-

†To whom correspondence should be addressed.
E-mail: xpfawd@nefu.edu.cn

ture consisting of multilayer graphene, which contains numerous oxygen-containing functional groups, have attracted enormous attention as a new support material for spinel ferrite for PMS activation [15,16]. Herein, confining $CuFe_2O_4$ nanoparticles in MWCNTs was fabricated for a novel catalyst that can prevent aggregation between particles and improve the dispersion of metal oxidants [17]. In addition, due to their immense specific surface areas, high chemical and thermal stability, extraordinary mechanical resistance, and superior chelating property with metal oxides, MWCNTs can facilitate catalytic performance to a great extent [9]. Most importantly, the excellent electrical conductivity and electron mobility of MWCNTs can not only accelerate interfacial electron transfer during catalytic reactions, but also stabilize the reactive intermediate to improve catalytic efficiency [18].

In this study, MWCNT-$CuFe_2O_4$ nanoparticles were synthesized through a hydrothermal method, and the properties of the nanoparticles were determined via a series of characterization methods. Next, various reaction systems were compared in terms of the removal performance of LEV, and the removal efficiency of LEV in the MWCNTs-$CuFe_2O_4$/PMS system was investigated under the influence of operational factors. Subsequently, quenching experiments and electron paramagnetic resonance (EPR) tests were utilized to identify the dominant active species and investigate the activation mechanism in the MWCNTs-$CuFe_2O_4$/PMS system. Furthermore, the reusability and stability of the catalyst were tested in five consecutive reaction cycles, and the mineralization degree of LEV was investigated with the TOC monitoring method. Finally, the degradation intermediates of LEV were identified by liquid chromatography-mass spectrometry (LC-MS), and possible degradation pathways were suggested in the MWCNTs-$CuFe_2O_4$/PMS system.

## MATERIALS AND METHODS

### 1. Synthesis of MWCNTs-$CuFe_2O_4$

MWCNTs-$CuFe_2O_4$ nanocomposites were fabricated through a hydrothermal method [15]. Initially, 2.42 g of $Cu(NO_3)_2{\cdot}3H_2O$ and 8.08 g of $Fe(NO_3)_3{\cdot}9H_2O$ were dispersed simultaneously in 30 mL of ultrapure water, followed by the addition of 1.3 g of MWCNTs to synthesize MWCNTs-$CuFe_2O_4$ with a mass ratio of approximately 3 : 1 (namely, MWCNTs-$CuFe_2O_4$ (1 : 3)). The above solution was treated with ultrasound for 15 min at room temperature and then stirred vigorously, and 4 $mol{\cdot}L^{-1}$ NaOH was added dropwise to adjust the solution pH to approximately 10. The mixture was further stirred continuously for 45 min under a magnetic stirrer. The precursor solution was transferred to a 50 mL sealed Teflon-lined stainless-steel autoclave and maintained in an oven for 12 h at 180 °C. The obtained precipitate was cooled naturally and washed several times using ultrapure water. Finally, the precursor was dried at 80 °C for 12 h and then ground to obtain MWCNTs-$CuFe_2O_4$ (1 : 3) in the form of a powder. For comparison of the catalytic efficiency of catalysts with different mass ratios and no MWCNT addition, the amount of $Cu(NO_3)_2{\cdot}3H_2O$ and $Fe(NO_3)_3{\cdot}9H_2O$ was fixed, while the dosage of MWCNTs was only varied using the same preparation methodology.

### 2. Materials Characterization

The surface morphology and structure of MWCNTs-$CuFe_2O_4$ (1 : 3) nanocomposites were characterized via scanning electron microscope (Su8020, Hitachi, Japan). Fourier transform infrared spectroscope (Nicolet IS10 FTIR, America thermo-electricity company) with the 0.4 $cm^{-1}$ resolution was employed to detect the structural components and the surface functional groups of $CuFe_2O_4$, fresh and used MWCNTs-$CuFe_2O_4$ (1 : 3) catalysts in the range 400-4,000 $cm^{-1}$. The phase structural analysis of $CuFe_2O_4$ material and various mass ratios of resultant MWCNTs-$CuFe_2O_4$ catalysts were observed with X-ray powder diffractometer (TD-3500, Dandong, China) equipped with Cu K$\alpha$ radiation and $\lambda$=0.15406 nm. Raman spectra were collected to obtain the structure defects and crystallization degree of MWCNTs and synthetic catalyst by Renishaw via Raman microscope with a 532 nm laser excitation from an Ar laser. A vibrating sample magnetometer (VSM, Quantum Design, America) was utilized for evaluating the magnetic properties of $CuFe_2O_4$ and fresh MWCNTs-$CuFe_2O_4$ (1 : 3) catalysts. $N_2$ adsorption-desorption isotherms and the distribution of pore size were detected, and the surface area, pore volume and pore size of MWCNTs, fresh and used MWCNTs-$CuFe_2O_4$ (1 : 3) were calculated using the Brunauer-Emmett-Teller (BET) method by the $N_2$ adsorption-desorption system (ASAP 2460).

Thermal-gravimetric analyzer (JY-TGAT10, Shanghai) was utilized to investigate the thermal transformation behavior and the MWCNTs content of MWCNTs-$CuFe_2O_4$ (1 : 3) catalyst from room temperature to 800 °C at 10 °C·$min^{-1}$ of the heating rate. The elemental composition and valence state of fresh and used nanocomposites were researched by X-ray photo-electron spectroscopy (XPS, Thermo Escalab 250 Xi, America), equipped with Al K$\alpha$ radiation (14.8 kV, 1.6 A). The UV-vis spectrophotometer (UV-1800, HACH, America) was applied for obtaining the LEV concentration at the maximum characteristic wavelength of 294 nm. The electron paramagnetic resonance spectra of the free radicals were collected on the electron paramagnetic resonance (EPR) spectrometer (A300-10/12, Bruker, Germany). Total organic carbon (TOC) content was measured to evaluate the mineralization degree during reactions based on TOC-LCPN Analyzer (TD-3500, Dandong, China). The degradation intermediates of LEV were detected with liquid chromatography mass spectrometry (LC-MS, Thermo Fisher Scientific, America).

### 3. Experimental Procedure

The bath experiments were carried out in 250 mL conical flasks, which were placed in a thermostatic oscillator (HZQ-C, China) at 160 r·$min^{-1}$ with a constant reaction temperature of 20 °C to obtain a homogeneous solution. In the experiment, 50 mL of LEV solution with a specific concentration was transferred into a conical flask, the prespecified concentration of PMS (50 mL) was dispersed into the above solution, and then the addition of MWCNTs-$CuFe_2O_4$ (1 : 3) with an appropriate dosage could immediately initiate the reaction to remove LEV. At the defined time interval, 3 mL of suspension was withdrawn from the reactor using a syringe and quickly filtered through a 0.45 μm filter for subsequent residual LEV concentration analysis at the maximum absorption wavelength of 294 nm via a UV-vis spectrophotometer. Specifically, many different system experiments containing various mass ratios of MWCNT-$CuFe_2O_4$ catalysts were conducted.

Under a similar experimental procedure, the effects of catalyst

dosage, PMS concentration, initial LEV concentration and initial solution pH (3-11) on the removal of LEV were investigated. In addition, the performance of catalysts for LEV removal was examined with the coexistence of various anions and HA at different concentrations. Quenching experiments were conducted to detect the types of active species generated in the MWCNTs-$CuFe_2O_4$/PMS (1 : 3) system using p-BQ, FFA, EtOH and TBA as effective scavengers. To evaluate the recyclability and stability of the MWCNT-$CuFe_2O_4$ (1 : 3) catalyst, five consecutive reaction cycles were performed under the same experimental conditions. After each reaction was finished, the used catalysts were recovered with an external magnet, cleaned using ultrapure water many times to remove adsorbed LEV molecules, dried in an oven at 80 °C for 4 h, and then reused in the subsequent catalytic runs [11]. The concentration of leached ions after the reaction was detected by an ICPOES730 inductively coupled plasma optical emission spectrometer (ICP-OES, Agilent, USA). Finally, the degradation intermediates were detected with LC-MS to propose the possible LEV degradation pathways. All experiments were performed in triplicate, and the average values are reported with error bars.

## RESULTS AND DISCUSSION

### 1. Characterization of the Catalyst

1-1. SEM

High-resolution SEM images with different magnifications were obtained, and the corresponding results are shown in Fig. 1a-d. As shown in Fig. 1a and b, the fresh $CuFe_2O_4$ nanoparticles exhibited an irregular spherical structure with an uneven size, and the MWCNTs twisted together in the form of a frizzy tubular structure. Obviously, a string of spherical particles was irregularly coated on the outer surface of the MWCNTs, indicating the successful modification of the $CuFe_2O_4$ nanoparticles on the MWCNTs. Furthermore, some of the $CuFe_2O_4$ nanoparticles accumulated to form larger clusters,

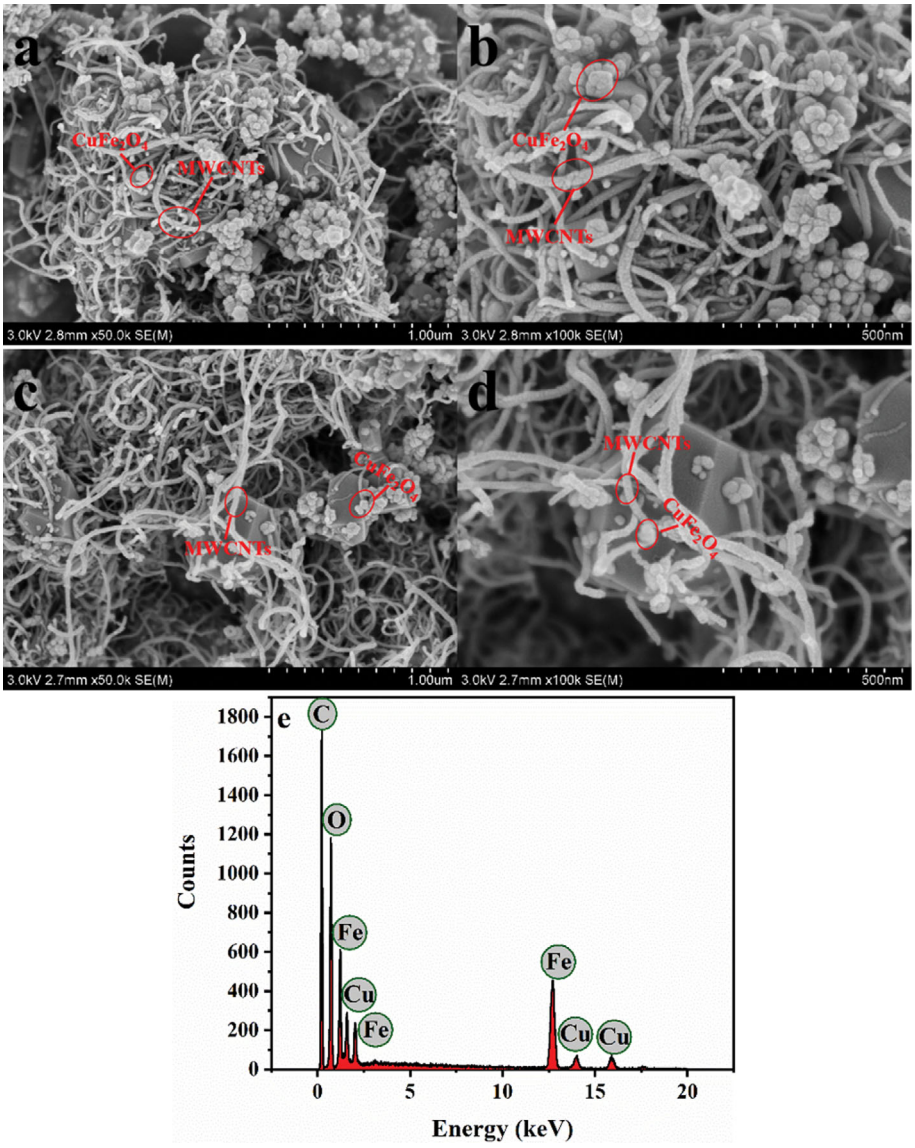


**Fig. 1. SEM images of fresh (a and b), used (c and d) MWCNTs-$CuFe_2O_4$ (1 : 3), and EDS spectrum (e) of MWCNTs-$CuFe_2O_4$ (1 : 3).**

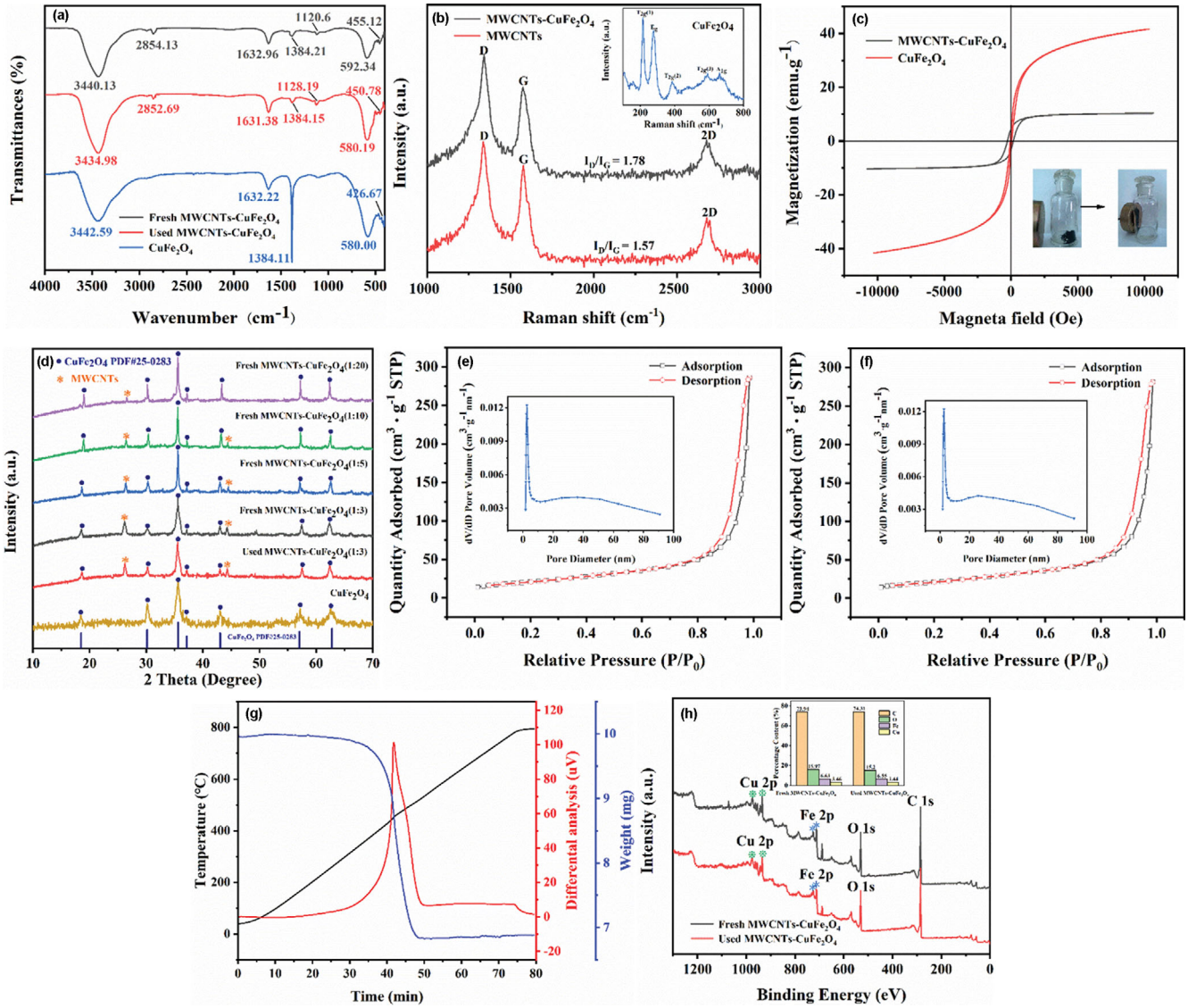


**Fig. 2. (a) FTIR spectra of $CuFe_2O_4$, fresh and used MWCNTs-$CuFe_2O_4$ (1 : 3); (b) Raman spectra of MWCNTs, MWCNTs-$CuFe_2O_4$ (1 : 3) and $CuFe_2O_4$ (insert); (c) VSM curves of $CuFe_2O_4$ and MWCNTs-$CuFe_2O_4$ (1 : 3); (d) XRD patterns of $CuFe_2O_4$, fresh and used MWCNTs-$CuFe_2O_4$; $N_2$ adsorption-desorption isotherms and the pore size distribution curves of fresh (e) and used (f) MWCNTs-$CuFe_2O_4$ (1 : 3); (g) TG curves of MWCNTs-$CuFe_2O_4$ (1 : 3); (h) XPS spectra of fresh and used MWCNTs-$CuFe_2O_4$ (1 : 3).**

and the MWCNTs-$CuFe_2O_4$ (1 : 3) nanomaterials had a rough surface, which may have been caused by the oxygen-containing groups on the outer wall of the MWCNTs. Obviously, a large number of pores between the MWCNTs-$CuFe_2O_4$ (1 : 3) nanocomposites appeared, providing sufficient reaction sites and facilitating the adsorption of LEV molecules. As shown in Fig. 1c and d, the used nanocatalysts did not undergo further aggregation or $CuFe_2O_4$ shedding, which may be ascribed to the strong interaction between the support materials and $CuFe_2O_4$. Using SEM-Nano Measurer, the diameter of the MWCNTs was approximately 25 nm, and the average size of $CuFe_2O_4$ was also on the nanoscale with a particle diameter less than 40 nm. In addition, EDS analysis was conducted to investigate the chemical composition of the catalyst, and the results are shown in Fig. 1e. The presence of C, O, Fe, and Cu confirmed the successful preparation of MWCNT-$CuFe_2O_4$ (1 : 3) nanoparticles.

1-2. FTIR

The mid-infrared region of the FTIR spectrum with the wavenumber range (400-4,000 $cm^{-1}$) was applied to qualitatively detect the specific chemical structure of bare $CuFe_2O_4$ and fresh and used MWCNTs-$CuFe_2O_4$ (1 : 3), and the results are presented in Fig. 2(a). The FTIR spectrum of the $CuFe_2O_4$ sample clearly shows two characterized absorption peaks at approximately 400-600 $cm^{-1}$ for all spinel-type compounds [19,20]. The peak at approximately 580 $cm^{-1}$ belongs to the stretching vibrations of $Fe^{3+}$-$O^{2-}$ tetrahedral complexes presented at A sites, and the peak at approximately 425 $cm^{-1}$ belongs to that of $Cu^{2+}$-$O^{2-}$ octahedral complexes present at B sites [21,22]. Additionally, the peaks observed above could also be observed in the FTIR spectra of fresh and MWCNTs-$CuFe_2O_4$ (1 : 3), which confirms the successful loading of $CuFe_2O_4$ onto the MWCNTs and the unchanged chemical structure of the $CuFe_2O_4$ samples.

As shown in the FTIR spectra of the three nanocomposites, two broad absorption bands at approximately 3,440 $cm^{-1}$ and 1,632 $cm^{-1}$ are ascribed to the O-H stretching and bending vibrations of hydroxyl groups [23] and the C=O asymmetric stretching vibrations of carboxylic groups [24]. The existence of hydroxyl and carboxylic groups could increase the hydrophilicity and dispersibility of catalysts, facilitating the adsorption of target pollutants and the uniformity of the catalytic reaction. A sharp peak at approximately 1,384 $cm^{-1}$ in the $CuFe_2O_4$ FTIR spectrum is related to the O-H stretching vibration from the surface-adsorbed species of particles [25]. Furthermore, the above peak of fresh and used as-synthesized catalysts became weaker and smaller to some degree, which is indicative of the interaction between $CuFe_2O_4$ and MWCNTs. In addition, the band at approximately 1,120 $cm^{-1}$ verifies the formation of C-O stretching vibrations derived from the carboxylic groups [26]. The coarse surface of MWCNTs was further confirmed by the presence of the outer hydroxyl and carboxylic functional groups, providing active sites for the immobilization of $CuFe_2O_4$ particles. The stability of the as-synthesized MWCNTs-$CuFe_2O_4$ (1 : 3) nanocomposite was also indicated by the small difference between the fresh and used MWCNTs-$CuFe_2O_4$ (1 : 3) FTIR spectra.

1-3. Raman Spectra

Fig. 2(b) presents the Raman spectra of pristine MWCNTs and MWCNT-$CuFe_2O_4$ (1 : 3) nanocomposites, and three significant peaks located at approximately 1,340 $cm^{-1}$ (D band), 1,575 $cm^{-1}$ (G band) and 2,680 $cm^{-1}$ (2D band) were observed. The D band represents the breathing mode of $A_{1g}$ symmetrical k-point photons, which is induced with a disorder vibrational mode and arises from $sp^3$ hybridized, amorphous carbon or defective graphene. The G band is assigned to the first-order scattering of the $E_{2g}$ phonons of well-ordered $sp^2$ bonded graphitic carbons, which indicates an in-planar stretching tangential mode and is observed in all graphene. In addition, the 2D band corresponds to the second-order two-phonon mode in the graphene sheet, which is a characteristic feature of high-quality graphene.

The relative intensity ratio of both the D band and G band ($I_D/I_G$) is a sensitive index that is commonly utilized to investigate the defect intensity and the degree of crystallization in carbon materials [27]. In comparison with the $I_D/I_G$ value (1.57) of pristine MWCNTs, that of MWCNTs-$CuFe_2O_4$ (1 : 3) was increased and determined to be 1.78. The increased $I_D/I_G$ values of doped MWCNTS are attributed to the decrease in the $sp^2$ cluster based on the destruction of $sp^3$ hybrids and the enhancement of the D band signal based on the restoration of numerous graphitic domains [28,29]. These results demonstrate that the defect and disorder degree of MWCNTs-$CuFe_2O_4$ (1 : 3) increased, which is good for the adsorption of pollutants and thus facilitates the kinetic process of pollutant removal. Furthermore, it is clearly observed that the 2D intensity of MWCNTs-$CuFe_2O_4$ (1 : 3) weakened compared to that of pure MWCNTs, demonstrating that the layer number of the graphene nanosheets showed a decreasing tendency [30]. This was possibly assigned to the strong coupling effect via some chemical bonds between MWCNTs and $CuFe_2O_4$. As shown in the inset in Fig. 2(b), the Raman spectra of $CuFe_2O_4$ in the range of 100-800 $cm^{-1}$ correspond to the $T_{2g}(1)$, $E_g$, $T_{2g}(2)$, $T_{2g}(3)$, and $A_{1g}$ vibration modes [30-32]. Based on the above Raman spectral analysis, the MWCNTs-$CuFe_2O_4$ (1 : 3) nanocomposites were prepared successfully through the hydrothermal method.

1-4. VSM

As shown in Fig. 2(c), the $CuFe_2O_4$ and MWCNTs-$CuFe_2O_4$ (1 : 3) all presented typical magnetic hysteresis (M-H) loops, which indicates the existence of ordered magnetic domains of spinel-type ferrite [33,34]. It was noted that the VSM measurement of all samples showed the superparamagnetic nature in which magnetization values increased with increasing applied field, which is a unique feature of spinel ferrite. As observed, the maximal magnetization value (Ms) of MWCNTs-$CuFe_2O_4$ (1 : 3) (10.35 $emu \cdot g^{-1}$) was lower than that of $CuFe_2O_4$ particles (41.61 $emu \cdot g^{-1}$), which might be due to the introduction of nonmagnetic MWCNTs in the MWCNTs-$CuFe_2O_4$ (1 : 3) nanocomposites. The distance between particles increased with the presence of MWCNTs, which effectively restricted the interparticle magnetic interactions and particle agglomeration. Furthermore, the coercivity (Hc) and remanence (Mr) of the MWCNT-$CuFe_2O_4$ (1 : 3) nanocomposites were 235 Oe and 4.32 $emu \cdot g^{-1}$, respectively, while those of $CuFe_2O_4$ were all near zero. The Hc and Mr values are related to the magnetic domains, crystal size and defect degree of magnetic materials. As observed in the inset of Fig. 2(c), MWCNT-$CuFe_2O_4$ (1 : 3) nanocomposites could be easily and quickly collected on one side using an external magnet near the glass bottle, which indicates that synthesized nanocomposites could be applied as recyclable catalysts to remove target pollutants during water remediation.

1-5. XRD

As seen in Fig. 2(d), all the fabricated samples show characteristic diffraction peaks at approximately 18.5°, 30.2°, 35.5°, 37.1°, 43.1°, 57.2°, and 62.5°, which match well with the (111), (220), (311), (222), (400), (422), (511) and (440) planes of the face-centered cubic spinel $CuFe_2O_4$ phase with space group Fd-3m (JCPDS 25-0283) [3]. Based on these results, the $CuFe_2O_4$ sample was successfully fabricated, and the presence in the MWCNTs-$CuFe_2O_4$ nanocomposites with various mass ratios was validated. Notably, the peaks of $CuFe_2O_4$ standard diffraction patterns in the MWCNT-$CuFe_2O_4$ samples were narrower than those in bare $CuFe_2O_4$, which indicates a relatively high crystallization degree of the MWCNT-$CuFe_2O_4$ nanocomposite and particle aggregation during the synthesis [35]. It should be emphasized that the intensity of the $CuFe_2O_4$ standard diffraction peaks in the MWCNT-$CuFe_2O_4$ XRD patterns also gradually weakened with increasing MWCNT content, which can be due to the dual status of MWCNTs, including the reducing agent and loading matrix.

Furthermore, two new characteristic diffraction peaks were observed that were conspicuously distributed from $CuFe_2O_4$ in the MWCNT-$CuFe_2O_4$ XRD patterns. A relatively strong peak at approximately $2\theta$ of 26.3° was indexed to the (002) planes of MWCNTs with a hexagonal graphite structure, while the other weaker peak at approximately 44.3° for MWCNTs corresponded to the (110) planes of crystalline carbon with the P63/mmc space group, which indicates that the carbon skeletons of the MWCNT support were not destroyed during the synthesis [36,37]. Other impurity diffraction peaks of single or mixed Cu-containing and Fe-containing oxides were not observed, indicating the high phase purity of the synthesized samples. In addition, the intensity and position of the

diffraction peaks in MWCNTs-$CuFe_2O_4$ (1 : 3) remained almost unchanged, showing that the crystal structure of the catalysts was relatively stable after the catalytic reaction.

Based on Scherrer's equation (Eq. (1)) [21], the average crystallite sizes of the above samples, namely, fresh and used MWCNTs-$CuFe_2O_4$ (1 : 3), fresh MWCNTs-$CuFe_2O_4$ (1 : 5), (1 : 10), (1 : 20), and bare $CuFe_2O_4$, were calculated to be 20.02 nm, 20.18 nm, 34.73 nm, 57.84 nm, 64.83 nm, and 70.05 nm, respectively.

$$D = \frac{0.98\lambda}{\beta\cos\theta} \quad (1)$$

where D (nm) is the nanoparticle diameter, $\lambda$ (nm) is the wavelength of the Cu K$\alpha$ radiation, $\beta$ (radians) is the full width at half-maximum and $\theta$ is the diffraction angle.

According to these results, the average crystallite sizes gradually increased with the reduction of MWCNTs, which was related to the nucleation rate of MWCNTs. When the proportion of MWCNTs decreased, the mobility of $CuFe_2O_4$ was enhanced, which resulted in the nucleation rate of MWCNTs slowing, thereby being conducive to crystallite growth before the particles formed uniform sizes and shapes.

1-6. $N_2$ Adsorption-desorption Analysis

As shown in Fig. 2(e) and 2(f), the $N_2$ adsorption-desorption isotherms of fresh and used MWCNTs-$CuFe_2O_4$ (1 : 3) all belong to type IV isotherms with H3 hysteresis loops at relative pressure ($P/P_0$) from 0.8 to 1.0, indicating that the as-prepared samples are irreversible desorption materials with mesoporous structures. The presence of a mesoporous structure in the above catalysts would accelerate the free mass transport of oxidants and substrates and provide more available active sites for redox reactions [38]. Moreover, the pore size distribution curves were calculated from isotherms using the Barrett-Joyner-Halenda method (insert in Fig. 2(e) and 2(f)), suggesting that the pore size distribution was relatively centered with effective pores ranging from 2 nm to 25 nm, which further confirmed the mesoporous properties of the resultant catalysts. Furthermore, the specific surface area, pore volume and pore size of pure MWCNTs and fresh and used MWCNTs-$CuFe_2O_4$ (1 : 3) were estimated by the Brunauer-Emmett-Teller method. The calculated specific surface area and pore volume of MWCNTs were 248.36 $m^2 \cdot g^{-1}$ and 1.45 $cm^3 \cdot g^{-1}$, respectively, which were much higher than those of fresh MWCNTs (74.24 $m^2 \cdot g^{-1}$ and 0.43 $cm^3 \cdot g^{-1}$) and MWCNTs-$CuFe_2O_4$ (1 : 3) (73.67 $m^2 \cdot g^{-1}$ and 0.42 $cm^3 \cdot g^{-1}$), which was probably due to the partial loading of $CuFe_2O_4$ on the inside wall of MWCNTs. In addition, the pore sizes of the MWCNTs and fresh and used MWCNTs-$CuFe_2O_4$ (1 : 3) were similar, 23.91 nm, 22.64 nm and 23.23 nm, respectively. The existence of no remarkable changes in the above characterization analysis of fresh and used MWCNTs-$CuFe_2O_4$ (1 : 3) indicates the highly stable framework of MWCNTs and the extreme stability of the as-prepared catalysts. Overall, it is reasonable to assume that MWCNTs are fantastic supporting materials based on their large specific surface area and that MWCNTs-$CuFe_2O_4$ (1 : 3) possesses excellent porosity and small pore size, which could reduce the mass transfer resistance and thus boost the activation efficiency during the reaction.

1-7. TG

The TG curve of dry MWCNT-$CuFe_2O_4$ (1 : 3) samples was utilized to investigate the thermal stability of nanocatalysts and to quantify the weight fraction of MWCNTs incorporated on the MWCNT-$CuFe_2O_4$ (1 : 3) nanocomposites. According to Fig. 2(g), the total weight was almost unchanged below 300 °C, which indicates that there was no physically absorbed water or interlayered water molecules [39]. When the heating temperature exceeded 300 °C, the weight began to decline slightly, and the mass loss of approximately 3.8% between 300 °C and 400 °C was mainly attributed to the improved crystallinity of the catalysts. It can be clearly observed that the TG curve of samples presented a super obvious exothermic peak at approximately 400-500 °C, which corresponded to conspicuous mass losses that were ascribed to the combustion of MWCNTs among the MWCNTs-$CuFe_2O_4$ (1 : 3) nanocomposites. As the temperature rose above 500 °C, the samples reached a constant mass of approximately 6.88 mg. Based on TG thermograms, $CuFe_2O_4$ present in nanocomposites would not be decomposed, and the content of MWCNTs in MWCNT-$CuFe_2O_4$ (1 : 3) samples was estimated to be approximately 30%.

1-8. XPS

A wide XPS spectrum was obtained to detect the elemental valence states and chemical bonding configuration of fresh and used MWCNT-$CuFe_2O_4$ (1 : 3) nanocomposites. As demonstrated in Fig. 2(h), the full spectrum XPS measurement confirmed the existence of elemental Cu, Fe, O, and C and calculated their respective contents (inset in Fig. 2(h)). It can be clearly seen that no other impurity elements were detected in the wide range of nanocomposites scans, and the content of each detected element did not change significantly, further indicating the high purity and excellent stability of the synthesized catalysts. It is noteworthy that the ratio of Fe/Cu in the fresh and used catalysts was approximately 1.9, which is lower than that of the theoretical formula of $CuFe_2O_4$. This may be due to inadequate deposition of metal cations in the MWCNTs.

**2. Removal Efficiency of LEV in Different Systems**

To comprehensively assess the catalytic activity of the prepared materials on PMS activation for removing LEV, a series of comparative experiments were conducted with various reaction systems under similar conditions (initial LEV concentration of 15 $mg \cdot L^{-1}$; PMS concentration of 2 mM; catalyst dosage of 0.5 $g \cdot L^{-1}$). According to Fig. 3(a) and (b), an LEV removal efficiency of only 2.24% was achieved in the PMS system in the absence of any external catalysts, further confirming the critical effects of catalysts. The adsorption efficiency of LEV by pristine MWCNTs, $CuFe_2O_4$, and MWCNTs-$CuFe_2O_4$ (1 : 3) was 13.26%, 23.13%, and 11.62%, respectively, which suggests that MWCNTs with larger specific surface areas can provide more adsorption sites on the catalyst surface and facilitate the degradation of pollutants on the catalyst surface.

In the presence of PMS, the addition of MWCNTs and $CuFe_2O_4$ to the solution containing the target pollutants resulted in the removal of approximately half of the LEV molecules. This may be due to the electron transfer between MWCNTs and PMS to generate active species and the interaction of copper and iron inducing the radical reaction pathway [37,40]. Surprisingly, a huge improvement in the LEV removal efficiency of $CuFe_2O_4$ via MWCNT decoration with the simultaneous use of PMS was observed in comparison with $CuFe_2O_4$/PMS systems. It can be noted that the

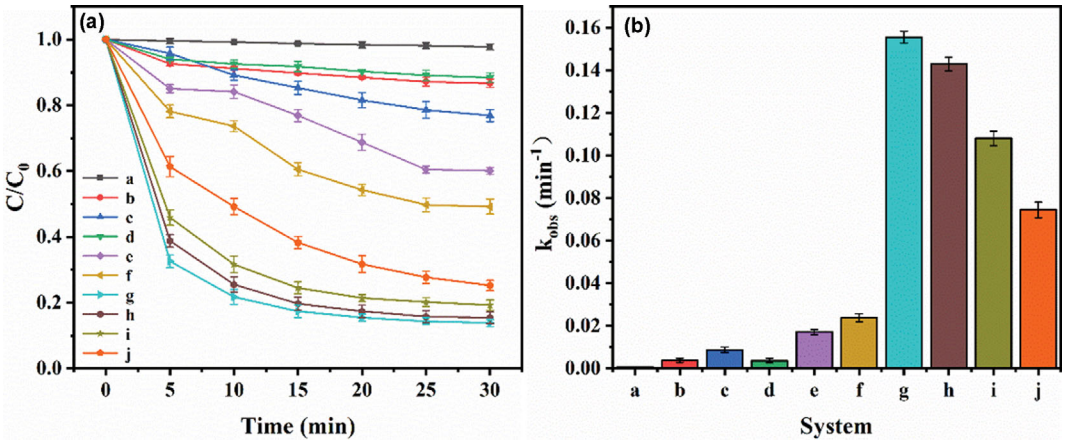


**Fig. 3. LEV removal efficiency (a) and kinetic constants (b) in different comparative systems. a: PMS; b: MWCNTs; c: $CuFe_2O_4$; d: MWCNTs-$CuFe_2O_4$ (1 : 3); e: MWCNTs/PMS; f: $CuFe_2O_4$/PMS; g: MWCNTs-$CuFe_2O_4$ (1 : 3)/PMS; h: MWCNTs-$CuFe_2O_4$ (1 : 5)/PMS; i: MWCNTs-$CuFe_2O_4$ (1 : 10)/PMS; j: MWCNTs-$CuFe_2O_4$ (1 : 20)/PMS.**

MWCNT-$CuFe_2O_4$ catalysts with different mass ratios can rapidly activate PMS to remove LEV during the initial reaction time. In addition, the adsorption capacity of MWCNTs-$CuFe_2O_4$ (1 : 3) was negligible compared with the catalytic contributions to the total LEV removal efficiency, which was intuitively observed in Fig. 3(a) and (b). Interestingly, the removal rates of LEV in MWCNTs-$CuFe_2O_4$ with different mass ratios/PMS systems were fitted using first-order kinetics and second-order kinetics (Eq. (2) and (3)), and the results were best fit by the second-order kinetic model, with correlation coefficient values ($R^2$) all above 0.9, as observed in Table S1. Taking the MWCNTs-$CuFe_2O_4$ (1 : 3)/PMS system, for example, its $k_{obs2}$ reached 0.1556 $min^{-1}$, which is 6.5 times that of the $CuFe_2O_4$/PMS system and 9.1 times that of the MWCNTs/PMS system, further confirming the results of the superior catalytic performance with nanocomposites. The excellent removal efficiency may be due to the synergistic effects between $CuFe_2O_4$ and MWCNTs [39] and the smaller average crystallite sizes compared with $CuFe_2O_4$, which in turn added to the available active sites based on the results of XRD analysis.

$$-\ln(C/C_0)=k_{obs1}t \quad (2)$$

$$1/C-1/C_0=k_{obs2}t \quad (3)$$

where $C_0$ ($mg\cdot L^{-1}$) represents the initial LEV concentration, C ($mg\cdot L^{-1}$) represents the LEV concentration at t (min), and $k_{obs1}$ and $k_{obs2}$ are the first- and second-order constant rates for LEV removal, respectively.

Additionally, the removal efficiency of MWCNT-$CuFe_2O_4$ with ratios of 1 : 3, 1 : 5, 1 : 10 and 1 : 20 was 86.18%, 84.56%, 80.75% and 74.78%, and the corresponding $k_{obs2}$ values were 0.01556, 0.143, 0.1081 and 0.0745 $min^{-1}$, respectively, which illustrated that the removal efficiencies decreased as the proportion of MWCNTs in the MWCNT-$CuFe_2O_4$ nanocomposites decreased. These results may be correlated with the fact that MWCNTs-$CuFe_2O_4$ (1 : 3) showed larger specific surface areas due to smaller average crystallite size, and fewer mass components of $CuFe_2O_4$ in the nanocomposites did not easily agglomerate [11,18]. All the above results indicate that MWCNTs-$CuFe_2O_4$ (1 : 3) shows excellent catalytic properties and a low adsorption effect and is a promising material to efficiently remove pollutants in the water purification field.

## 3. The Effects of Key Operating Factors on LEV Removal

### 3-1. Effect of Catalyst Dosage

Fig. 4(a) and (b) show the effect of different catalyst dosages on the LEV removal efficiency in the MWCNTs-$CuFe_2O_4$ (1 : 3)/PMS system with the other operational parameters held constant (PMS concentration of 2 mM; LEV initial concentration of 15 $mg\cdot L^{-1}$). As expected, the removal efficiency was obviously increased to 35.12% when the MWCNT-$CuFe_2O_4$ (1 : 3) catalyst was added into the solution with a dosage of 0.1 $g\cdot L^{-1}$ compared with the removal efficiency of only 2.24% in the control experiment without catalyst addition, which further indicated that the catalyst played a critical role in PMS activation. With the increase in catalyst dosage to 0.5 $g\cdot L^{-1}$, there was a sharp improvement trend in the LEV removal efficiency, increasing to 86.18%, and the corresponding $k_{obs2}$ values all showed the same trend, increasing to 0.1556 $min^{-1}$. In addition, with a further increase in MWCNT-$CuFe_2O_4$ (1 : 3) dosage from 1 $g\cdot L^{-1}$ to 1.5 $g\cdot L^{-1}$, the LEV removal efficiency increased slightly from 89.7% to 93.03%, while the $k_{obs2}$ values rose obviously from 0.1757 $min^{-1}$ to 0.2546 $min^{-1}$. The increase in the LEV removal efficiency could be attributed to the enhancement in the amount and availability of active sites on the catalyst surface with increasing catalyst dosage [7], which facilitated contaminant removal as well as PMS activation by inducing the production of more reactive species.

However, a further enhancement was hardly observed, especially in LEV removal efficiency, as the catalyst dosage increased to above 1.5 $g\cdot L^{-1}$. The almost fixed LEV removal efficiency may be because certain amounts of PMS had been fully activated by the catalyst with 1.5 $g\cdot L^{-1}$, causing the active species to not be produced continuously [41], and the agglomeration of catalyst nanoparticles reduced the specific surface areas of the catalyst. Yang et al. [1], who studied the degradation of LEV by the $CuFe_2O_4$/MMT-k10/PS system, found that 85.55% of LEV was degraded with 1.0 $g\cdot L^{-1}$ PS, 1.5 $g\cdot L^{-1}$ catalyst and 10 $mg\cdot L^{-1}$ LEV. Obviously, the catalytic system we designed is more effective in LEV degradation.

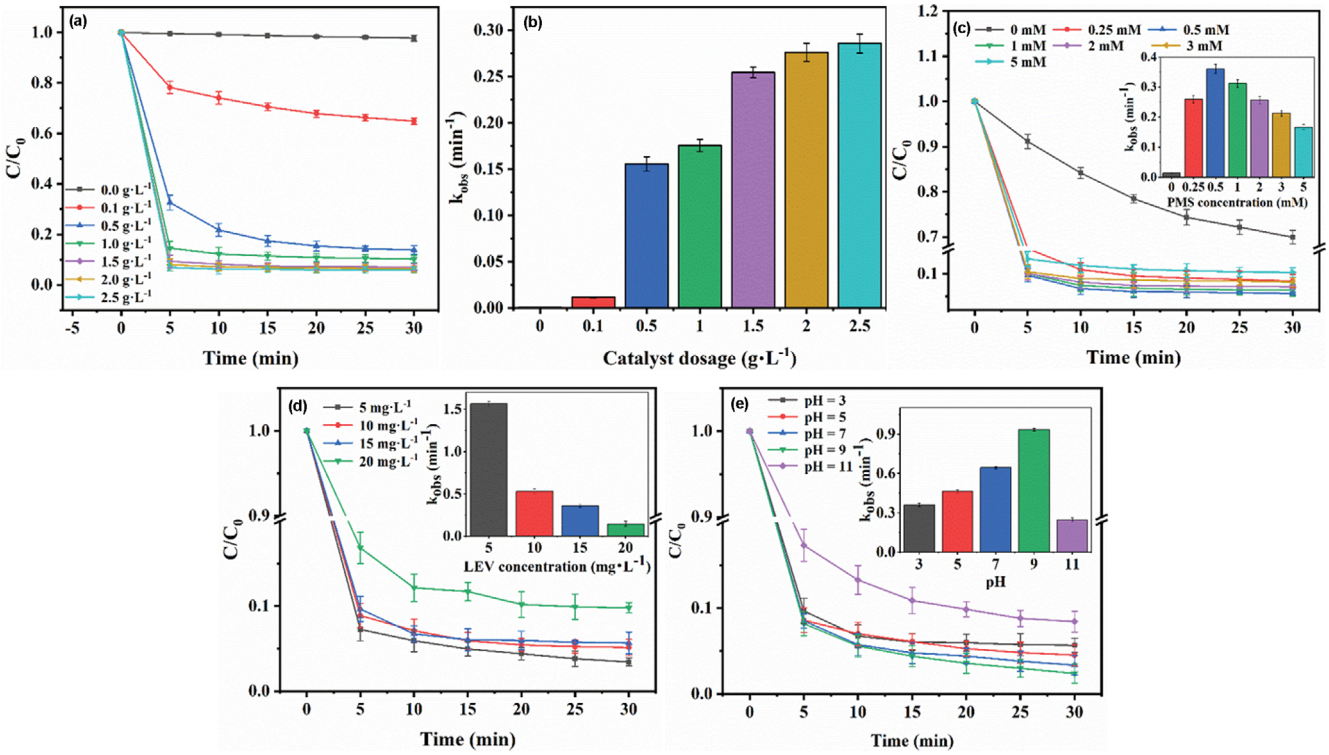


**Fig. 4. Effects of MWCNTs-$CuFe_2O_4$ (1 : 3) dosage ((a) and (b)), PMS concentration (c), LEV initial concentration (d) and the initial pH (e) on the LEV removal efficiency.**

3-2. Effect of PMS Concentration

A sufficient PMS concentration means greater collision between PMS and catalysts, which theoretically generates large amounts of reactive species [8]. As shown in Fig. 4(c), the effect of various PMS concentrations on the removal efficiency of LEV was investigated at an MWCNT-$CuFe_2O_4$ (1 : 3) dosage of 1.5 $g{\cdot}L^{-1}$ and an LEV initial concentration of 15 $mg{\cdot}L^{-1}$. Note that the addition of PMS into the reaction solution remarkably improved the LEV removal efficiency in comparison with the catalyst alone (control experiment), obtaining 30.09% removal efficiency, which confirms that PMS plays a vital role in producing active species to remove LEV. The LEV removal efficiency increased from 91.62% to 94.33% with increasing PMS concentration from 0.25 mM to 0.5 mM, and similarly, $k_{obs2}$ also increased from 0.2597 $min^{-1}$ to 0.3607 $min^{-1}$. However, upon further increasing the PMS concentration to above 0.5 mM, the LEV removal efficiency was dramatically suppressed, which can be explained by the fact that the active sites on the catalyst surface were fully occupied by PMS and were already saturated at a high PMS concentration of 0.5 mM, which cannot be activated by MWCNTs-$CuFe_2O_4$ (1 : 3) to produce more reactive species; the excessive PMS might quench $SO_4^{\cdot-}$ and hydroxyl radicals (·OH), inhibiting the LEV removal reaction (Eqs. (4) and (5)) [41], and the self-scavenging reaction of $SO_4^{\cdot-}$ might occur with a high concentration of PMS, further producing other species with weaker oxidation potential (Eq. (6)). Compared with the study conducted by Madihi-Bidgoli et al. [37], 0.9 mM PMS was chosen to degrade AZB, and the removal efficiency reached only 63.5%. The comparative results further show the higher efficiency of the system designed in this work.

$$HSO_5^- + SO_4^{\cdot-} \rightarrow HSO_4^- + SO_5^{\cdot-} \quad (4)$$

$$HSO_5^- + {\cdot}OH \rightarrow H_2O + SO_5^{\cdot-} \quad (5)$$

$$SO_4^{\cdot-} + SO_4^{\cdot-} \rightarrow S_2O_8^{2-} \quad (6)$$

3-3. Effect of Initial LEV Concentration

To investigate the effect of the initial LEV concentration in the MWCNTs-$CuFe_2O_4$ (1 : 3)/PMS system, experiments were conducted under other constant conditions (catalyst dosage of 1.5 $mg{\cdot}L^{-1}$ and PMS concentration of 0.5 mM), and the results are shown in Fig. 4(d). Apparently, the MWCNTs-$CuFe_2O_4$ (1 : 3)/PMS system all reached a high LEV removal efficiency, while the corresponding kinetic rate constants exhibited marked differences at various LEV initial concentrations.

In detail, the LEV removal efficiency decreased slightly from 96.56% at 5 $mg{\cdot}L^{-1}$ LEV to 94.86%, 94.33%, and 90.09% at 10, 15, and 20 $mg{\cdot}L^{-1}$ LEV, respectively. The $k_{obs2}$ values of LEV decreased significantly from 1.568 $min^{-1}$ to 0.1458 $min^{-1}$, in which the $k_{obs2}$ of the LEV initial concentration of 5 $mg{\cdot}L^{-1}$ was nearly 11 times higher than that of 20 $mg{\cdot}L^{-1}$ LEV. The decrease may be because when PMS and catalyst were all constant, the generation of active species was limited, and it was impossible to oxidize excessive LEV; in addition, intermediates with high concentrations were produced under high LEV initial concentration conditions, which could compete with target pollutant molecules to consume the constant amounts of active species [3,27].

3-4. Effect of Initial pH

The effect of different initial pH values (3, 5, 7, 9 and 11) on LEV removal was investigated at a catalyst dosage of 1.5 $g \cdot L^{-1}$, PMS concentration of 0.5 mM and LEV initial concentration of 15 $mg \cdot L^{-1}$, and the corresponding results are shown in Fig. 4(e). The removal efficiency of LEV under acidic, neutral and alkaline conditions was found to all reach greater than 90% within 30 min, indicating that the designed MWCNTs-$CuFe_2O_4$ (1 : 3)/PMS system could be operated in the reaction solution with a wide range of initial pH values. Note that the LEV removal efficiency increased from 94.33% to 97.62% with increasing initial pH from 3 to 9, and simultaneously, $k_{obs2}$ was also obviously improved from 0.3607 $min^{-1}$ to 0.9345 $min^{-1}$. However, a further increase in pH to 11 led to a decrease in the removal efficiency of LEV to 91.56%, which was confirmed by $k_{obs2}$ at pH 11 of 0.2471 $min^{-1}$.

In general, the effect of various initial pH values on LEV removal efficiency is related to the comprehensive influences of the point of zero charge ($pH_{pzc}$) of MWCNTs-$CuFe_2O_4$ (1 : 3), the $pK_{a2}$ of PMS, and the $pK_{a1}$ and $pK_{a2}$ of LEV [18,42]. Based on zeta potential analysis, the $pH_{pzc}$ of MWCNTs-$CuFe_2O_4$ (1 : 3) was approximately 8.6, meaning that the catalyst surface was protonated and that the surface charge was positive when the pH was lower than the $pH_{pzc}$. In contrast, when the pH was higher than $pH_{pzc}$, the surface of the catalyst was deprotonated and negatively charged. In addition, the existing forms of PMS depended on the solution pH, which was due to the PMS $pK_{a2}$ of 9.4, which mostly existed in the form of $HSO_5^-$ at pH values lower than 9.4, while it primarily existed in the form of $SO_5^{2-}$ at pH values higher than 9.4 [15]. According to the $pK_{a1}$ (5.7) and $pK_{a2}$ (7.9) of LEV, LEV was protonated into $LEV^+$ at pH<5.7, while LEV was deprotonated into $LEV^-$ at pH>7.9. In the pH range of 5.7-7.9, LEV existed as a zwitterion.

The increase in LEV removal efficiency from pH 3 to 9 might be due to the electrostatic attraction between $HSO_5^-$ and the protonated surface of the catalyst, accelerating the electron transport processes. In addition, LEV gradually presented an increasing amount of $LEV^-$, which was beneficial for electrostatic adsorption on the surface of MWCNTs-$CuFe_2O_4$ (1 : 3), thereby improving the probability of LEV removal. As the initial pH increased to 11, the decrease in LEV removal may be related to the fact that PMS ($SO_5^{2-}$) and deprotonated LEV were repulsed away from the catalyst surface due to a large number of negative charges; $SO_5^{2-}$ of the dominant PMS species had a low potential for the production of $SO_4^{\bullet-}$, which decreased the active species concentration; under strong alkaline conditions, PMS may be decomposed into sulfate ions and water through its nonradical pathways (Eq. (7)), and excessive $OH^-$ could scavenge $SO_4^{\bullet-}$ and further generate other reactive species with low oxidation potential (Eq. (8)).

$$HSO_5^- + SO_5^{2-} + OH^- \rightarrow 2SO_4^{2-} + O_2 + H_2O \quad (7)$$

$$OH^- + SO_4^{\bullet-} \rightarrow SO_4^{2-} + \cdot OH \quad (8)$$

3-5. Effects of Various Anions and HA

There are various coexisting substances, such as inorganic anions ($NO_3^-$, $HCO_3^-$, $CO_3^{2-}$, $H_2PO_4^-$, and $Cl^-$) and natural organic matter (NOM), in natural waters [43]; therefore, the effects of the above anions and NOM with different concentrations on the LEV removal efficiency were investigated to evaluate the applicability of the MWCNTs-$CuFe_2O_4$ (1 : 3)/PMS system under conditions including a catalyst dosage of 1.5 $g \cdot L^{-1}$, PMS concentration of 0.5 mM and LEV initial concentration of 15 $mg \cdot L^{-1}$. Interestingly, similar

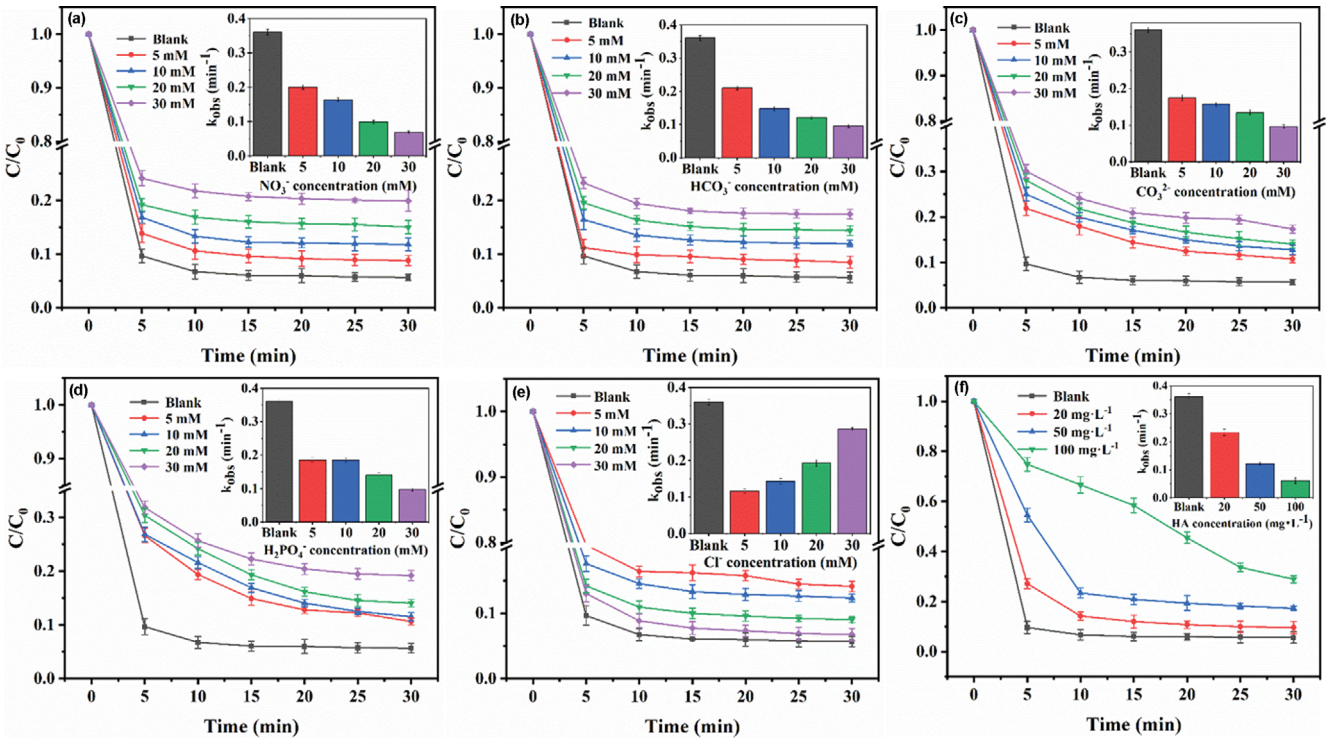


**Fig. 5. Effects of $NO_3^-$ (a), $HCO_3^-$ (b), $CO_3^{2-}$ (c), $H_2PO_4^-$ (d), $Cl^-$ (e) and HA (f) on the LEV removal efficiency.**

inhibitory effects on LEV removal were observed with the respective introduction of $NO_3^-$, $HCO_3^-$, $CO_3^{2-}$ and $H_2PO_4^-$ into the designed system (Fig. 5(a), (b), (c) and (d)), in which increasing these four anion concentrations aggravated the hindering effects. This phenomenon could be attributed to the scavenging effect of $SO_4^{\bullet-}$ and ·OH by anions and further generation of corresponding reactive species with low oxidation capacity for removing LEV [8,15], according to Eqs. (9)-(16). In addition, the inhibitory effect of $HCO_3^-$ could also be explained by the fact that the ionization of $HCO_3^-$ generated a certain amount of hydrogen ions, leading to a decrease in pH, which might hinder the PMS activation and LEV removal efficiency. Interestingly, another reason for the reduction of LEV removal in the case of $H_2PO_4^-$ was related to the fact that $H_2PO_4^-$ could deactivate the active centres of the catalyst surface via adsorption for metal oxides forming an inner-sphere complex [44].

$$NO_3^- + SO_4^{\bullet-} \rightarrow SO_4^{2-} + NO_3^{\bullet} \quad (9)$$

$$NO_3^- + \cdot OH \rightarrow OH^- + NO_3^{\bullet} \quad (10)$$

$$HCO_3^- + SO_4^{\bullet-} \rightarrow SO_4^{2-} + CO_3^{\bullet-} \quad (11)$$

$$HCO_3^- + \cdot OH \rightarrow OH^- + CO_3^{\bullet-} \quad (12)$$

$$CO_3^{2-} + SO_4^{\bullet-} \rightarrow SO_4^{2-} + CO_3^{\bullet-} \quad (13)$$

$$CO_3^{2-} + \cdot OH \rightarrow OH^- + CO_3^{\bullet-} \quad (14)$$

$$H_2PO_4^- + SO_4^{\bullet-} \rightarrow SO_4^{2-} + H_2PO_4^{\bullet} \quad (15)$$

$$H_2PO_4^- + \cdot OH \rightarrow OH^- + H_2PO_4^{\bullet} \quad (16)$$

Notably, the presence of $Cl^-$ showed a different effect on LEV removal, as shown in Fig. 5(e). The LEV removal efficiency and rate all dropped significantly from 94.33% to 85.89% and 0.3607 $min^{-1}$ to 0.1155 $min^{-1}$, respectively, as the $Cl^-$ concentration increased from 0 to 5 mM. This can be explained by two aspects: first, $Cl^-$ could react with reactive radical species to generate chlorine radicals with low oxidation potential compared with $SO_4^{\bullet-}$ and ·OH (Eqs. (17) and (18)); in addition, the direct reaction between $Cl^-$ and PMS molecules resulted in the production of reactive halogens to repress LEV removal (Eqs. (19) and (20)). However, the inhibition effect was gradually slight, with a continuous increase in $Cl^-$ concentration from 10 mM to 50 mM, which indicated that high levels of chlorine radicals could be generated at high concentration of $Cl^-$ and that these excess radicals were also capable of capturing LEV and then compensating for the consumption of the main radicals [37].

HA, as the most representative NOM indicator, was introduced into the MWCNTs-$CuFe_2O_4$ (1 : 3)/PMS system to investigate the influence on LEV removal, and the corresponding results are shown in Fig. 5(f). Note that the presence of HA (20, 50 and 100 $mg \cdot L^{-1}$) exhibited a negative effect on LEV removal efficiency, and the effect became more and more serious with increasing HA concentration. The inhibition effect might be because HA with abundant electron sites can serve as a radical scavenger by competing with LEV for $SO_4^{\bullet-}$ and ·OH; in addition, phenolic hydroxyl and carboxyl groups contained in HA can adsorb onto the catalyst surface and block reactive sites, which inhibits LEV removal in the MWCNTs-$CuFe_2O_4$ (1 : 3)/PMS system [45].

$$Cl^- + SO_4^{\bullet-} \rightarrow SO_4^{2-} + Cl^{\bullet} \quad (17)$$

$$Cl^- + \cdot OH \rightarrow ClOH^{\bullet-} \quad (18)$$

$$Cl^- + HSO_5^- \rightarrow SO_4^{2-} + HOCl \quad (19)$$

$$Cl^- + HSO_5^- \rightarrow HSO_4^- + OCl^- \quad (20)$$

## 4. The Activation Mechanisms of PMS in the MWCNTs-$CuFe_2O_4$ (1 : 3)/PMS System

### 4-1. Identification of Reactive Species

It is well known that the reaction rate constant between p-BQ and superoxide radicals ($\cdot O_2^-$) is (0.9-1)×$10^9$ $M^{-1}S^{-1}$, and the reaction rate constant between FFA and signal oxygen ($^1O_2$) is 1.2×$10^8$ $M^{-1}S^{-1}$ [47], which are employed to quench $\cdot O_2^-$ and $^1O_2$, respectively. In addition, EtOH is considered a simultaneous scavenger for $SO_4^{\bullet-}$ and ·OH because it has rate constants comparable to those of $SO_4^{\bullet-}$ ((1.6-7.8)×$10^7$ $M^{-1}S^{-1}$) and ·OH ((1.2-2.8)×$10^9$ $M^{-1}S^{-1}$) [48]. TBA is only utilized to quench ·OH because the reaction with ·OH is more efficient ((3.8-7.6)×$10^8$ $M^{-1}S^{-1}$) than that with $SO_4^{\bullet-}$ ((4.0-9.1)×$10^5$ $M^{-1}S^{-1}$) [49]. Consequently, the difference in LEV removal in the presence of EtOH and TBA reflects the contribution of $SO_4^{\bullet-}$ to PMS activation. As exhibited in Fig. 6(a), the LEV removal efficiency and rate were 94.33% and 0.3607 $min^{-1}$, respectively, in the original system without the addition of quenching agents. Surprisingly, the respective introduction of 2 mM p-BQ and 12.5 mM FFA to the reaction solution dramatically suppressed LEV removal, in which the removal efficiency decreased to 51.26% and 48.96% and the kinetic rate constants dropped to 0.0204 $min^{-1}$ and 0.022 $min^{-1}$, respectively, which indicates that $\cdot O_2^-$ and $^1O_2$ have important roles in PMS activation for LEV removal. As observed, the LEV removal efficiency only decreased to 84.24% in the presence of 50 mM EtOH in the reaction system, while a slight decrease in the LEV removal efficiency and rate was seen with the addition of 50 mM TBA, meaning that the contributions of $SO_4^{\bullet-}$ and ·OH to PMS activation were not significant.

EPR tests were conducted to further confirm the existence and variation of active species in the reaction system. 5,5-Dimethyl-1-pyrroline N-oxide (DMPO) was used to capture $\cdot O_2^-$, ·OH and $SO_4^{\bullet-}$, while 4-oxo-2,2,6,6,tetramethylpiperidine (TEMP) was utilized as spin trap agent of $^1O_2$. As shown in Fig. 6(b), c and d, the characteristic peaks of DMPO-$\cdot O_2^-$, TEMP-$^1O_2$, DMPO-$SO_4^{\bullet-}$ and DMPO-·OH adducts appeared in the EPR spectra, and the peak intensities of the above adducts all obviously increased with increasing reaction time from 1 to 5 min, which indicates the continuous production of active species during the PMS activation processes. Among them, a typical triplet signal with an intensity ratio of 1 : 1 : 1 of TEMP-$^1O_2$ was clearly observed. In addition, the four characteristic peaks of DMPO-·OH had intensity ratio of 1 : 2 : 2 : 1, and the six relatively weak peaks of DMPO-$SO_4^{\bullet-}$ were also monitored around the DMPO-·OH peak signal.

In summary, the results of quenching experiments and EPR tests indicate that the above four active species were all generated and that $\cdot O_2^-$ and $^1O_2$ were the primary active species in the MWCNT-$CuFe_2O_4$ (1 : 3)/PMS system, which indicates that PMS activation involves two kinds of mechanisms, including the nonfree radical

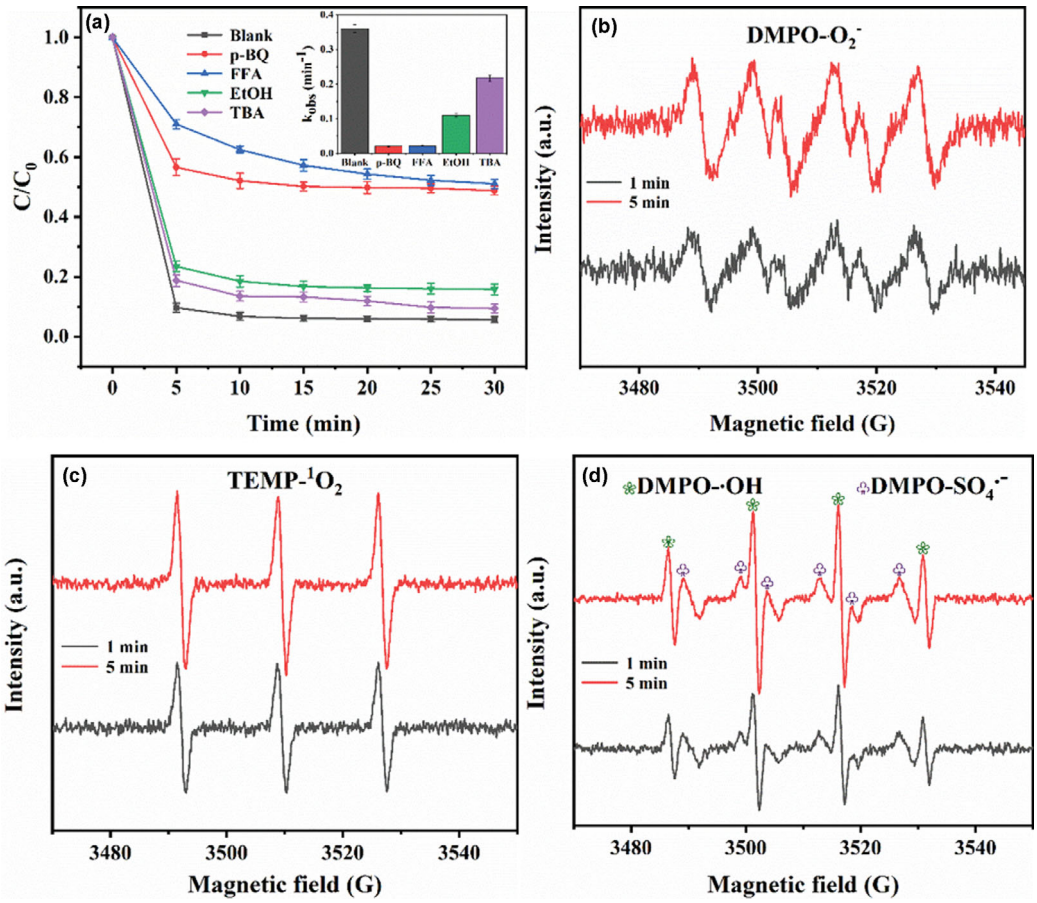


**Fig. 6. LEV removal in the presence of scavengers in the MWCNTs-$CuFe_2O_4$ (1 : 3)/PMS system (a), and the EPR spectra of $\cdot O_2^-$ (b); $^1O_2$ (c); $SO_4^{\cdot -}$ and ·OH (d).**

($^1O_2$) and free radical ($\cdot O_2^-$, $SO_4^{\cdot -}$ and ·OH) reaction pathways.

4-2. Chemical State of Elements on the Catalyst Surface

To better explore the PMS activation mechanism by MWCNTs-$CuFe_2O_4$ (1 : 3), the chemical state changes of elemental Cu, Fe, O and C on the composite surface before and after the catalytic reaction were analyzed by XPS, while the redox reaction of each metal ion during the reaction was speculated. The high-resolution Cu 2p XPS spectra (Fig. 7(a)) displayed one spin-orbit trebles centered at 940 eV and one spin-orbit doubles centered at 957 eV by using a Gaussian fitting method, which individually corresponded to the $2p_{3/2}$ and $2p_{1/2}$ peaks of Cu cations [50]. In detail, the Cu $2p_{3/2}$ lines can be split into three peaks at binding energies of 933.4, 941.8, and 945.2 eV attributed to $Cu^{2+}$ and $Cu^+$ on octahedral coordination sites and $Cu^{2+}$ on tetrahedral coordination sites, respectively. The doublets of Cu $2p_{1/2}$ binding energies at 955.3 and 962.5 eV were ascribed to the contributions from $Cu^{2+}$ on the octahedral sites and tetrahedral sites, respectively [12,20]. The relative contributions of $Cu^+$ and $Cu^{2+}$ to the overall Cu cation intensity were approximately 15% and 85%, respectively, of which the content of $Cu^{2+}$ on the tetrahedral sites decreased from 24% to 17% after the reaction, indicating the slight transformation of $Cu^{2+}$ coordination environment from tetrahedral sites to octahedral sites (Fig. S1(a)). The variation in the content of various Cu cations before and after the reaction indicates that Cu cations can act as PMS activation sites to participate in the reaction. Based on the Cu 2p spectrum, Cu cations mainly occupied the octahedral sites, which confirms that $CuFe_2O_4$ has a spinel structure and is consistent with the FTIR and Raman results.

In the slight asymmetry deconvoluted spectrum of Fe 2p (Fig. 7(b)), the Fe 2p orbit was fitted by two split-orbit peaks of a low energy band at 713.2 eV (Fe $2p_{3/2}$) and a high energy band at 725.4 eV (Fe $2p_{1/2}$) [51]. In addition, the spin separation energy between Fe $2p_{3/2}$ and Fe $2p_{1/2}$ was 12.2 eV, and one couple of shakeup satellites at approximately 716.2 and 719.4 eV were observed. The XPS of Fe 2p regions displayed two non-equivalent bonds of Fe cations in $CuFe_2O_4$ spinel materials, which was confirmed by the fact that $Fe^{3+}$ and $Fe^{2+}$ occupied two kinds of lattice sites (A-sites and B-sites) [13]. The doublets of the Fe $2p_{3/2}$ binding energies at 710.2 and 712.3 eV were ascribed to $Fe^{2+}$ and $Fe^{3+}$ on the octahedral coordination sites. The central peak of 714.1 eV in Fe $2p_{3/2}$ corresponded to $Fe^{3+}$ from tetrahedral sites. Furthermore, the Fe $2p_{1/2}$ binding energies at 723.8 and 726.4 eV were assigned to the contributions from $Fe^{3+}$ on octahedral and tetrahedral sites, respectively. Based on the relative contributions of $Fe^{2+}$ and $Fe^{3+}$ in different coordination environments to the overall intensity of Fe cations (Fig. S1(b)), the proportions of $Fe^{3+}$ on tetrahedral sites slightly increased from 34% to 43% before the reaction, while those of $Fe^{2+}$ on octahedral sites and $Fe^{3+}$ on tetrahedral sites decreased to

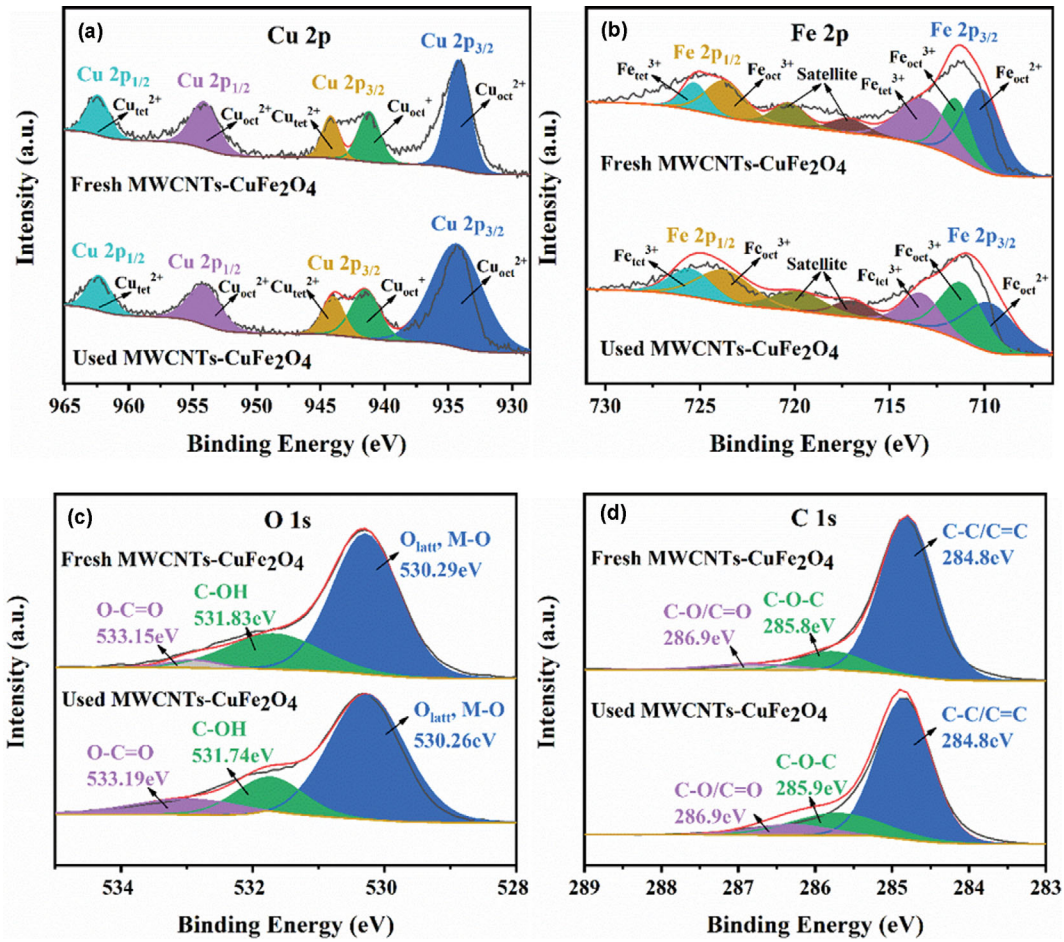


**Fig. 7. XPS spectra of Cu 2p (a), Fe 2p (b), O 1s (c) and C 1s (d) of fresh and used MWCNTs-$CuFe_2O_4$ (1 : 3).**

different degrees, indicating that PMS activation involved a single electron transfer mechanism in Fe cation centres. The presence of $Cu^+$ and $Fe^{2+}$ in relatively low proportions was attributed to the partial reduction of $Cu^{2+}$ and $Fe^{3+}$ during the synthesis and catalytic reaction processes.

The high-resolution O 1s spectrum (Fig. 7(c)) was deconvoluted into three representative peaks at approximately 530, 531, and 533 eV. The peak centered at 530 eV could be assigned to the bond energy of the metal-oxygen (M-O) band [52], which was assigned to the lattice oxygen signal ($O_{latt}$), further illustrating the interaction between $CuFe_2O_4$ and MWCNTs through chemical coordination bands. The latter two peaks at approximately 531 and 533 eV correspond to the C-OH and O-C=O bands, respectively [52, 53], indicating that the surface of the nanocomposites was hydroxylated and carboxylated. Fig. S1(c) shows that the content of $O_{latt}$ remained stable before and after the reaction, while content variations of C-OH and O-C=O bands were obviously observed, suggesting that C-OH tended to be converted to the more stable double carbon bonded with oxygen.

Moreover, as seen in Fig. 7(d), the C 1s spectrum was fitted by three peaks. The strong peak centered at 284 eV is ascribed to the $sp^3$-hybridized carbon C-C/C=C [54], while the weaker peaks centered at 285 and 286 eV were assigned to C-O-C ($sp^2$ carbon) and C-O/C=O [55], which indicates that oxygen from the $CuFe_2O_4$ structure was successfully inserted into the MWCNT structure and further formed various oxygen-containing functional groups on the MWCNT surface. As depicted in Fig. S1(d), the proportion of C-C/C=C ($sp^3$ carbon) dropped from 84% to 73% after the PMS activation reaction, suggesting that the bond might be consumed through some pathway as an effective functional group during the catalytic reaction. In addition, the C-O-C content slightly increased by 9% relative to the overall intensity of the C contents, which was due to the further oxidation of the MWCNTs during the PMS activation processes. The presence of the above bonds indicates the chemical combination of MWCNTs and $CuFe_2O_4$ and provides anchoring sites for metal cations.

4-3. The Generative Mechanism of Reactive Species

The results of quenching and EPR experiments confirmed that active species, including $\cdot O_2^-$, $^1O_2$, $SO_4^{\cdot-}$ and ·OH, could be generated in the MWCNTs-$CuFe_2O_4$ (1 : 3)/PMS system; that is, PMS activation involves a free radical pathway and a nonfree radical pathway. In addition, the XPS spectra indicate the existence of abundant functional groups on the MWCNT surface and the coexistence of Cu and Fe ions with different valences. According to the discussion of the above results, the possible mechanisms of PMS activation for LEV removal with MWCNT-$CuFe_2O_4$ (1 : 3) catalysts were

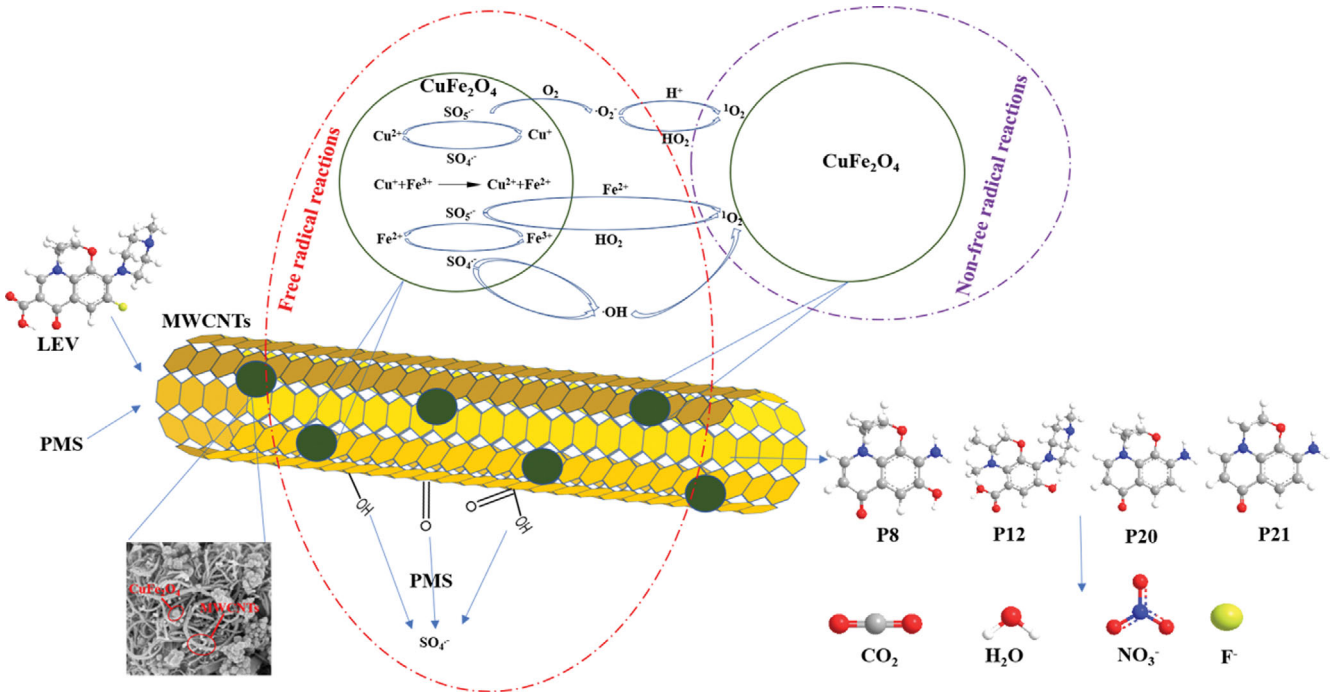


**Fig. 8. The possible mechanisms of PMS activation by MWCNTs-$CuFe_2O_4$ (1 : 3) for LEV removal.**

propounded (Fig. 8). At first, PMS was adsorbed adequately on the catalyst surface because of the adsorption capacity of the catalyst. In the free radical pathway, PMS, acting as an electron donor, transferred a single electron to $Cu^{2+}$ and $Fe^{3+}$, which resulted in the production of $SO_5^{\bullet-}$ and the reduction of $Cu^{2+}$ and $Fe^{3+}$ (Eqs. (21) and (22)). Simultaneously, the reverse electron transfer from $Cu^{+}$ and $Fe^{2+}$ to PMS could produce active $SO_4^{\bullet-}$ species and regenerate Cu and Fe ions with high valence (Eqs. (23) and (24)).

It is notable that $Fe^{3+}$ was able to capture one electron from $Cu^{+}$, in which the reaction was thermodynamically feasible ($E_0Fe^{3+}/Fe^{2+}$=0.77 V, $E_0Cu^{2+}/Cu^{+}$=0.17 V), maintaining the continuous formation of active species (Eq. (25)). $SO_4^{\bullet-}$ can directly react with $H_2O$ or $OH^-$ to generate ·OH (Eqs. (26) and (27)). In addition, $O_2$ could be formed under the decomposition of $SO_5^{\bullet-}$ and further accept a single electron from the catalytic cycle of metal ions to produce $\cdot O_2^-$ (Eqs. (28) and (29)). MWCNTs with highly electronic conductive properties not only supported $CuFe_2O_4$ particles as frameworks, but were also conducive to the surface electron transfer between metal ions as the electron mediator. More importantly, PMS could be efficiently activated by the surface groups of MWCNTs to generate the extra electron (Eqs. (30)-(32)), and this was attributed to the fact that the abundant surface groups favored PMS activation, also resulting in the more rapid in-situ interfacial formation of reactive species via an electron transfer mechanism. In the other nonfree radical pathway, PMS activation mainly depended on the active species of $^1O_2$, which was produced by the reaction between $\cdot O_2^-$ and $H^+$ or $H_2O$ or ·OH (Eqs. (33)-(35)). Furthermore, $SO_5^{\bullet-}$ could react with $Fe^{2+}$ or $H_2O$ to generate $^1O_2$ for PMS activation through a nonfree radical pathway (Eqs. (36) and (37)). Finally, LEV molecules were attacked with congenerous effects between the free radical pathway and the nonfree radical pathway to generate intermediate products, which were eventually degraded to $CO_2$ and $H_2O$ (Eq. (38)).

$$Cu^{2+}+HSO_5^-\rightarrow Cu^{+}+SO_5^{\bullet-}+H^+ \quad (21)$$

$$Fe^{3+}+HSO_5^-\rightarrow Fe^{2+}+SO_5^{\bullet-}+H^+ \quad (22)$$

$$Cu^{+}+HSO_5^-\rightarrow Cu^{2+}+SO_4^{\bullet-}+OH^- \quad (23)$$

$$Fe^{2+}+HSO_5^-\rightarrow Fe^{3+}+SO_4^{\bullet-}+OH^- \quad (24)$$

$$Fe^{3+}+Cu^{+}\rightarrow Fe^{2+}+Cu^{2+} \quad (25)$$

$$SO_4^{\bullet-}+H_2O\rightarrow \cdot OH+SO_4^{2-}+H^+ \quad (26)$$

$$SO_4^{\bullet-}+OH^-\rightarrow \cdot OH+SO_4^{2-} \quad (27)$$

$$2SO_5^{\bullet-}\rightarrow 2SO_4^{\bullet-}+O_2 \quad (28)$$

$$O_2+e^-\rightarrow \cdot O_2^- \quad (29)$$

$$HSO_5^-+[MWCNTs_{surf\text{-}COOH}]\rightarrow SO_4^{\bullet-}+[MWCNTs_{surf\text{-}COO\cdot}]+H_2O \quad (30)$$

$$HSO_5^-+[MWCNTs_{surf\text{-}OH}]\rightarrow SO_4^{\bullet-}+[MWCNTs_{surf\text{-}O\cdot}]+H_2O \quad (31)$$

$$HSO_5^-+[MWCNTs_{surf\text{-}C=O}]\rightarrow SO_4^{\bullet-}+[MWCNTs_{surf\text{-}CO\cdot}]+OH^- \quad (32)$$

$$2\cdot O_2^-+2H^+\rightarrow H_2O_2+{}^1O_2 \quad (33)$$

$$\cdot O_2^-+2H_2O\rightarrow H_2O_2+{}^1O_2+2OH^- \quad (34)$$

$$\cdot O_2^-+\cdot OH\rightarrow {}^1O_2+OH^- \quad (35)$$

$$Fe^{2+}+SO_5^{\bullet-}\rightarrow Fe^{3+}+SO_4^{2-}+{}^1O_2 \quad (36)$$

$$SO_5^{\bullet-}+0.5H_2O\rightarrow HSO_4^-+0.75{}^1O_2 \quad (37)$$

$$\text{LEV+free radicals/non-free radical}\rightarrow\text{intermediate products}\rightarrow CO_2+H_2O \quad (38)$$

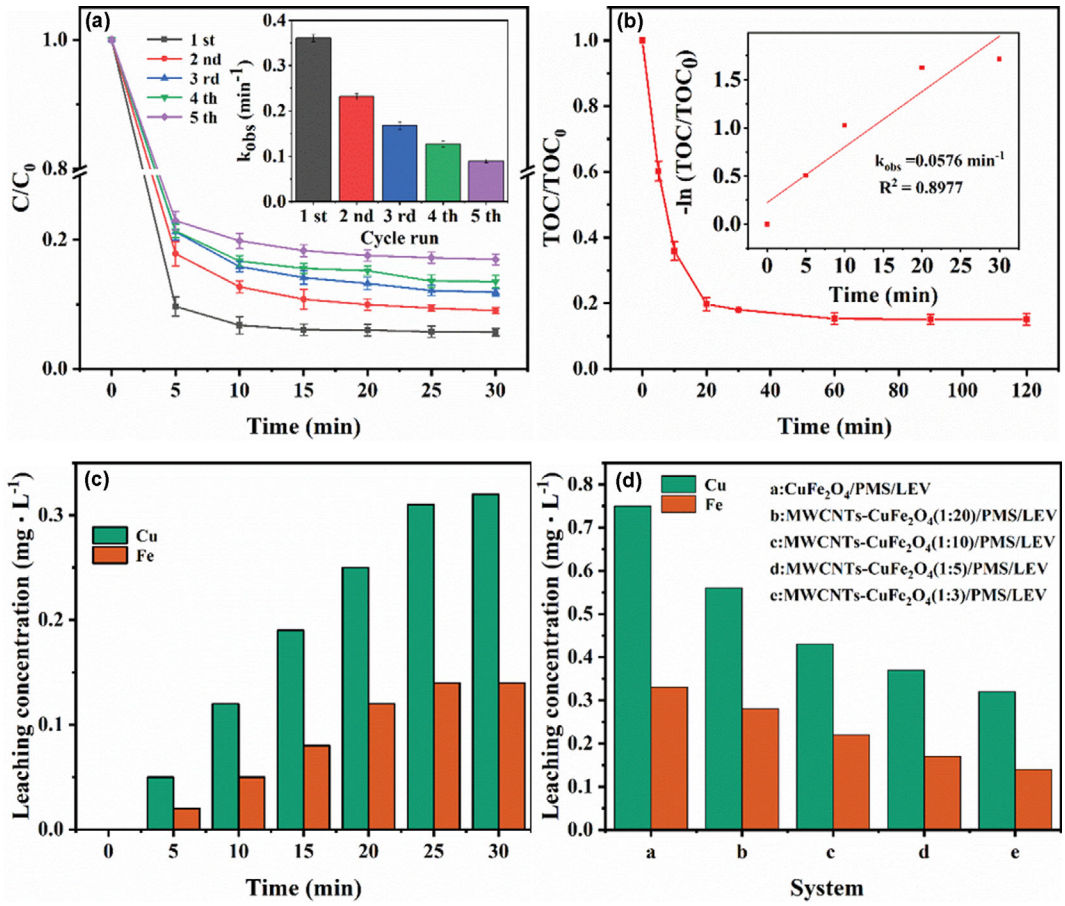


**Fig. 9. The catalytic efficiency of MWCNTs-$CuFe_2O_4$ (1 : 3) for LEV removal after five consecutive runs (a), the TOC removal efficiency (b), the metal ions leaching in MWCNTs-$CuFe_2O_4$ (1 : 3)/PMS/LEV system (c), and the leaching amounts of metal ions in different catalytic systems (d).**

## 5. The Stability of MWCNTs-$CuFe_2O_4$ (1 : 3) and the Mineralization of LEV

The stability and mineralization ability of the designed catalysts is critical for practical application; hence, five consecutive reaction cycles and TOC removal experiments were performed under the same conditions, including a catalyst dosage of 1.5 $g \cdot L^{-1}$, PMS concentration of 0.5 mM and LEV initial concentration of 15 $mg \cdot L^{-1}$. Herein, the recycled catalysts were collected magnetically, cleaned with ultrapure water multiple times and finally dried in an oven at 80 °C for 4 h for the subsequent catalytic reaction.

As shown in Fig. 9(a), a slight decrease in LEV removal efficiency from 94.33% to 90.97%, 88.15%, 86.48% and 83.06% was observed with increasing cycle number. The slight decrease in LEV removal could be due to the occupancy of reactive sites on the catalyst surface by the intermediates of LEV and the leakage of catalysing ions. Note that the LEV removal efficiency in the five recycling processes all remained above 80%, indicating that the synthesized catalysts had excellent catalyst activity and stability. The result of LEV mineralization is shown in Fig. 9(b). The TOC removal efficiency and rate surprisingly reached 82% and 0.0576 $min^{-1}$ at 30 min, respectively, suggesting that LEV molecules could be effectively mineralized by the designed catalytic system into $CO_2$ and $H_2O$.

## 6. Leaching of Metal Ions from the Catalyst During the Reaction

The concentration of metal ions leached into the solution at the end of the catalytic degradation reaction was detected by an inductively coupled plasma optical emission spectrometer (reaction conditions: catalyst dosage of 1.5 $g \cdot L^{-1}$, PMS concentration of 0.5 mM and LEV initial concentration of 15 $mg \cdot L^{-1}$). As shown in Fig. 9(c), the total amounts of Cu and Fe leached increased gradually as the reaction time increased. Furthermore, the results (Fig. 9(d)) show that when MWCNT-$CuFe_2O_4$ (1 : 3) was used as the catalyst, the leaching concentration of Cu and Fe was 0.32 $mg \cdot L^{-1}$ and 0.14 $mg \cdot L^{-1}$, respectively, lower than those of Cu (0.75 $mg \cdot L^{-1}$) and Fe (0.33 $mg \cdot L^{-1}$) when $CuFe_2O_4$ was used as the catalyst alone. Compared with $CuFe_2O_4$-$MoS_2$ [56], which was also used to activate PMS, MWCNTs-$CuFe_2O_4$ (1 : 3) prepared in this research showed a lower metal ion leaching rate in the catalytic degradation reaction. In addition, this leaching concentration was much lower than the standard limits stipulated in China's environmental quality standards for surface water. The results indicate that the composite catalyst can effectively reduce the concentration of metal ions leached into the solution and reduce the risk of secondary pollution to the environment. The outstanding contribution of the introduction of MWCNTs in reducing the metal ion leaching problem was confirmed.

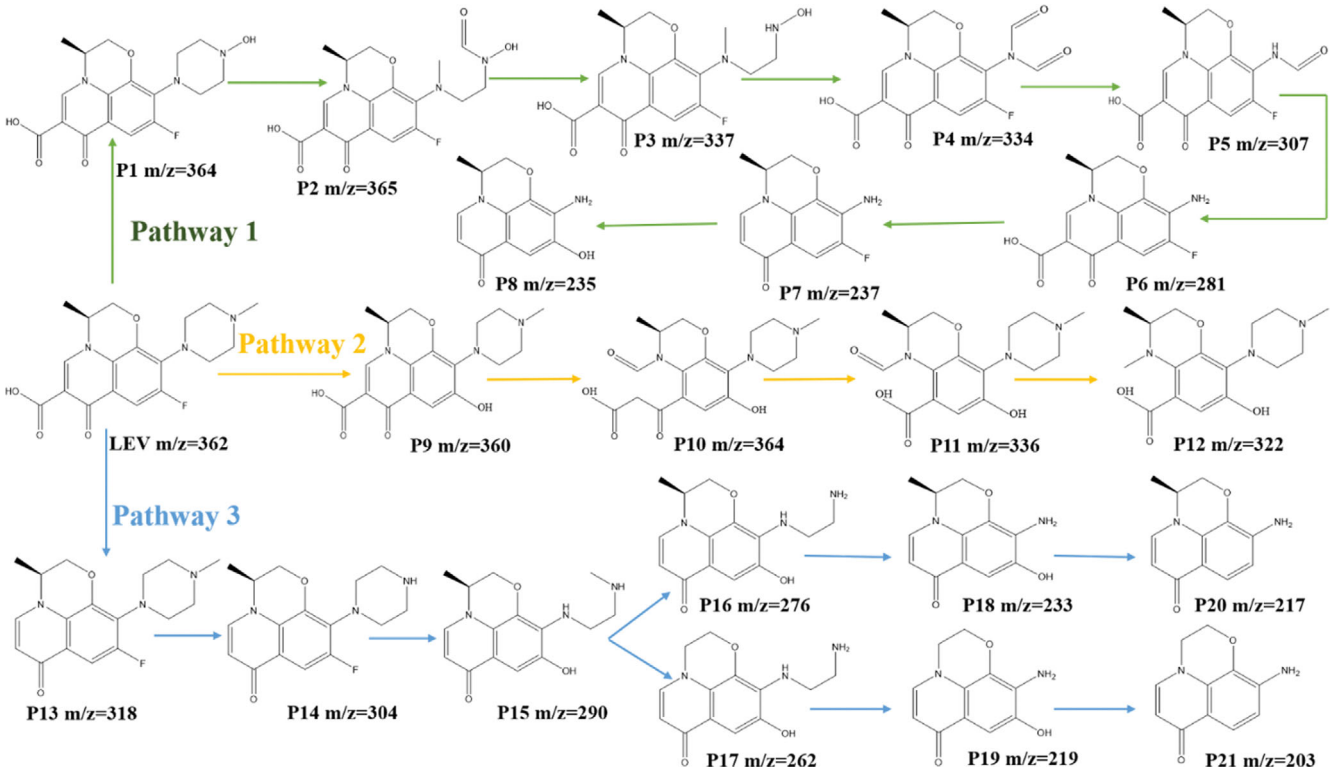


**Fig. 10. The possible degradation pathways of LEV in MWCNTs-$CuFe_2O_4$ (1 : 3)/PMS system.**

### 7. The Degradation Pathways of LEV

A total of 21 intermediate products of LEV in the MWCNTs-$CuFe_2O_4$ (1 : 3)/PMS system were detected using the LC-MS technology (Table S2), and the structures of intermediate products were determined based on the fragmentation patterns and previous literature. The possible LEV degradation pathways are proposed as illustrated in Fig. 10. Under the attack of active species, LEV undergoes the oxidation of quinolone ring, defluorination, hydroxylation, decarboxylation, demethylation, carbonylation and decarbonylation reaction, which were summarized into three branching pathways.

In pathway 1, the N-methyl group on the piperazine ring of LEV is first substituted by hydroxyl group to from P1 [57]. P1 undergoes ring-opening reaction to produce P2. Then P3 and P4 are produced from P2 through decarbonylation and oxidation [58]. Continuous decarbonylation reaction of P4 leads to the generation of P5 and P6. P7 is generated by the decarboxylation of P6 and finally forms P8 through the replacement of the F atom by the hydroxyl group [59]. In pathway 2, LEV is first defluorinated with the attack of hydroxyl group to from P9. The quinolone ring of P9 can be easily disrupted by reactive oxygen species to form P10 [60], which generates P11 and P12 through decarboxylation and deoxygenation reactions, respectively. In pathway 3, the parent LEV undergoes decarboxylation and demethylation to generate P13 and P14, respectively. The break of piperazinyl ring and the replacement of F atom by hydroxyl group results in the production of P15 [61]. Subsequently, the formation of P16 and P17 is attributed to demethylation of P15. The nitrogen atom on the piperazinyl ring from P16 and P17 is attacked by active species, resulting in the generation of P18 and P19, which are dehydroxylated to form P20 and P21 [62], respectively. In view of TOC removal efficiency, it could be concluded that all these intermediate products in the MWCNTs-$CuFe_2O_4$ (1 : 3)/PMS system are further degraded into smaller compounds with less molecular weight, and finally mineralized to $CO_2$, $H_2O$, $NO_3^-$, and $F^-$ as the reaction progresses.

## CONCLUSION

MWCNT-$CuFe_2O_4$ (1 : 3) nanoparticles with excellent chemical structure were fabricated using a hydrothermal method and utilized to activate PMS for ultraefficient LEV removal compared with other catalysts. Two PMS activation pathways were proposed involving free radical and nonfree radical pathways, of which superoxide radicals and signal oxygen were the main active species, and the surface groups of MWCNTs played a part in the generation of reactive species. Overall, the designed heterogeneous advanced oxidation process promotes the effective combination of spinel ferrite and one-dimensional nanomaterials and realizes the synergistic activation of PMS with sustainability and stability. This study provides new ideas for the design of high-performance multiphase catalysts for applications in catalytic oxidation and offers new insights into the investigation of the mechanism. Due to the profound PMS activation with MWCNTs, further study is warranted. The activation technology is expected to be further extended for the treatment of other kinds of organic pollutants or to introduce synthetic catalysts into membrane technology to optimize the water treatment process, which will provide broader prospects for its practical applica-

tion. In addition, not only the removal efficiency of pollutants but also the overall investment and operation costs should be considered in practical applications, in which reducing operating costs is an important challenge.

## ACKNOWLEDGEMENTS

This work was supported by the Heilongjiang Provincial Natural Science Foundation of China (LH2019D002).

## CONFLICT OF INTEREST

The authors declare no conflict of interest.

## SUPPORTING INFORMATION

Additional information as noted in the text. This information is available via the Internet at http://www.springer.com/chemistry/journal/11814.

## REFERENCES

1. J. Y. Yang, M. Y. Huang, S. S. Wang, X. Y. Mao, Y. M. Hu and X. Chen, *Water*, **12**, 3583 (2020).
2. Y. W. Zhong, K. Shih, Z. H. Diao, G. Song, M. H. Su, L. A. Hou, D. Y. Chen and L. J. Kong, *Chem. Eng. J.*, **417**, 129225 (2021).
3. J. Zhao, P. F. Xiao, S. Han, M. Zulhumar and D. D. Wu, *Water Sci. Technol.*, **85**, 645 (2022).
4. A. Czyrski, K. Anusiak and A. Teżyk, *Sci. Rep.*, **9**, 1 (2019).
5. X. J. Wen, C. G. Niu, H. Guo, L. Zhang, C. Liang and G. M. Zeng, *J. Catal.*, **358**, 211 (2018).
6. R. Anjali and S. Shanthakumar, *J. Environ. Manage.*, **246**, 51 (2019).
7. S. Han and P. F. Xiao, *Sep. Purif. Technol.*, **287**, 120533 (2022).
8. Q. R. Wang, Y. X. Shi, S. Y. Lv, Y. Liang and P. F. Xiao, *RSC Adv.*, **11**, 18525 (2021).
9. P. F. Xiao, L. An and D. D. Wu, *New Carbon Mater.*, **35,** 667 (2020).
10. L. An and P. F. Xiao, *RSC Adv.*, **10**, 19401 (2020).
11. R. B. Li, M. X. Cai, Z. J. Xie, Q. X. Zhang, Y. Q. Zeng, H. J. Liu and W. Y. Lv, *Appl. Catal. B.*, **244**, 974 (2019).
12. A. Lassoued, M. Ben Hassine, F. Karolak, B. Dkhil, S. Ammar and A. Gadri, *J. Mater. Sci. Mater. Electron.*, **28**, 18857 (2017).
13. K. Atacan, N. Güy and M. Özacar, *J. Colloids Interface Sci. Commun.*, **40**, 100359 (2021).
14. K. Atacan, *J. Alloys Compd.*, **791**, 391 (2019).
15. Z. Q. Yang, Y. Li, X. Y. Zhang, X. D. Cui, S. He, H. Liang and A. Ding, *Chem. Eng. J.*, **384**, 123319 (2020).
16. H. Pourzamani, E. Jafari, M. Rozveh, H. Mohammadi, M. Rostami and N. Mengelizadeh, *Desalin. Water Treat.*, **167**, 156 (2019).
17. K. Zhu, Q. Bin, Y. Q. Shen, J. Huang, D. D. He and W. J. Chen, *Chem. Eng. J.*, **402**, 126090 (2020).
18. B. M. Liu, W. B. Song, H. X. Wu, Z. Y. Liu, Y. J. Sun, Y. H. Xu and H. L. Zheng, *Chem. Eng. J.*, **398**, 125498 (2020).
19. L. K. Wu, H. Wu, H. B. Zhang, H. Z. Cao, G. Y. Hou, Y. P. Tang and G. Q. Zheng, *Chem. Eng. J.*, **334**, 1808 (2018).
20. P. Laokul, V. Amornkitbamrung, S. Seraphin and S. Maensiri, *Curr. Appl. Phys.*, **11**, 101 (2011).
21. Y. B. Wang, H. Y. Zhao, M. F. Li, J. Q. Fan and G. H. Zhao, *Appl. Catal., B.*, **147**, 534 (2014).
22. A. Dandia, A. K. Jain and S. Sharma, *RSC Adv.*, **3**, 2924 (2013).
23. A. Samadi, R. Ahmadi and S. M. Hosseini, *Org. Electron.*, **75**, 105405 (2019).
24. E. M. Elsehly, N. G. Chechenin, A. V. Makunin, H. A. Motaweh, K. A. Bukunov and E. G. Leksina, *J. Nanomater.*, **6**, 2 (2016).
25. Z. Y. Lu, M. He, L. L. Yang, Z. F. Ma, L. Yang, D. D. Wang, Y. S. Yan, W. D. Shi, Y. Liu and Z. F. Hua, *RSC Adv.*, **5**, 47820 (2015).
26. G. H. Liu, C. Li, B. A. Stewart, L. Liu, M. Zhang, M. Y. Yang and K. F. Lin, *Chem. Eng. J.*, **399**, 125722 (2020).
27. S. Z. Wang and J. L. Wang, *Chem. Eng. J.*, **356**, 350 (2019).
28. J. Kang, X. J. Duan, L. Zhou, H. Q. Sun, M. O. Tade and S. B. Wang, *Chem. Eng. J.*, **288**, 399 (2016).
29. S. M. Li, B. Wang, J. H. Liu and M. Yu, *Electrochim. Acta*, **129**, 33 (2014).
30. P. X. Li, R. G. Ma, Y. Zhou, Y. F. Chen, Z. Z. Zhou, G. H. Liu, G. H. Peng and J. C. Wang, *RSC Adv.*, **5**, 44476 (2015).
31. N. Kumar, A. Kumar, G. M. Huang, W. W. Wu and T. Y. Yseng, *Appl. Surf. Sci.*, **433**, 1100 (2018).
32. H. Y. Gao, J. J. Xiang and Y. Cao, *Appl. Surf. Sci.*, **413**, 351 (2017).
33. A. Manikandan, M. Durka, S. A. Antony and J. Supercond, *Nov. Magn.*, **28**, 2047 (2015).
34. A. Manikandan, M. Durka and S. A. Antony, *J. Supercond. Nov. Magn.*, **27**, 2841 (2014).
35. Y. L. Zou, Z. Y. Li, Y. L. Liu, J. L. Duan and B. Long, *J. Alloys Compd.*, **820**, 153085 (2020).
36. W. L. Guo, Z. H. Zhang, H. Lin and L. Cai, *Mol. Catal.*, **492**, 111011 (2020).
37. S. Madihi-Bidgoli, S. Asadnezhad, A. Yaghoot-Nezhad and A. Hassani, *J. Environ. Chem. Eng.*, **9**, 106660 (2021).
38. X. L. Li, H. J. Lu, Y. Zhang and F. He, *Chem. Eng. J.*, **316**, 893 (2017).
39. T. J. Al-Musawi, G. McKay, P. Rajiv, N. Mengelizadeh and D. Balarak, *J. Photoch. Photobio.*, A **424**, 113617 (2022).
40. B. Kakavandi, S. Alavi, F. Ghanbari and M. Ahmadi, *Chemosphere*, **287**, 132024 (2022).
41. M. Alhamd, T. Tabatabaie, I. Parseh, F. Amiri and N. Mengelizadeh, *Environ. Sci. Pollut. Res.*, **28**, 57099 (2021).
42. T. j. Al-Musawi, P. Rajiv, N. Mengelizadeh, F. S. Arghavan and D. Balarak, *J. Mol. Liq.*, **337**, 116470 (2021).
43. X. J. Wen, Q. Lu, X. X. Lv, J. Sun, J. Guo, Z. H. Fei and C. G. Niu, *J. Hazard. Mater.*, **385**, 121508 (2020).
44. M. M. Amini and N. Mengelizadeh, *Environ. Sci. Pollut. Res.*, **27**, 45324 (2020).
45. X. L. Zeng, J. Chen, R. J. Qu, M. B. Feng and Z. Y. Wang, *Chem. Eng. J.*, **319**, 98 (2017).
46. M. J. Huang, S. S. Peng, W. Xiang, C. Wang, X. H. Wu, J. Mao and T. Zhou, *Chem. Eng. J.*, **429**, 132372 (2022).
47. C. H. Shen, Y. Chen, X. J. Xu, X. Y. Li, X. J. Wen, Z. T. Liu, R. Xing, H. Guo and Z. H. Fei, *J. Hazard. Mater.*, **416**, 126217 (2021).
48. Y. M. Qi, R. J. Qu, J. Q. Liu, J. Chen, G. Al-Basher, N. Alsultan, Z. Y. Wang and Z. L. Huo, *Chemosphere*, **237**, 124484 (2019).
49. J. Y. Yao, Y. Yu, R. J. Qu, J. Chen, Z. L. Huo, F. Zhu and Z. Y. Wang, *Environ. Sci. Technol.*, **54**, 9052 (2020).
50. Y. Y. Wang, L. Yao, X. Liu, J. Cheng, W. Liu, T. Liu, M. M. Sun, L. J. Zhao, F. Ding, Z. W. Lu, P. Zou, X. X. Wang, Q. B. Zhao and H. B.

Rao, *Biosens. Bioelectron*., **142**, 111483 (2019).
51. L. C. Yue, S. G. Zhang, H. Q. Zhao, F. Yu, M. Wang, L. L. An, X. D. Zhang and J. Mi, *Solid State Ion*., **329**, 15 (2019).
52. X. F. Yu, G. Y. Chen, Y. Z. Wang, J. W. Liu, K. Pei, Y. H. Zhao, W. B. You, L. Wang, J. Zhang, L. S. Xing, J. J. Ding, G. Z. Ding, M. Wang and R. C. Che, *Nano Res*., **13**, 437 (2020).
53. Z. X. Wang, Y. F. Han, W. L. Fan, Y. X. Wang and L. H. Huang, *Sep. Purif. Technol*., **278**, 119558 (2021).
54. B. M. Liu, W. B. Song, H. X. Wu, Z. Y. Liu, Y. Teng, Y. J. Sun, Y. H. Xu and H. L. Zheng, *Chem. Eng. J*., **398**, 125498 (2020).
55. B. M. Liu, W. B. Song, W. W. Zhang, X. Zhang, S. L. Pan, H. X. Wu, Y. J. Sun and Y. H. Xu, *Sep. Purif. Technol*., **273**, 118705 (2021).
56. R. Bai, W. F. Yan, Y. Xiao, S. Q. Wang, X. C. Tian, J. P. Li, X. F. Xiao, X. Q. Lu and F. Zhao, *Chem. Eng. J*., **397**, 125501 (2020).
57. W. T. Tan, Y. Ruan, Z. H. Diao, G. Song, M. H. Su, L. A. Hou, D. Y. Chen, L. J. Kong and H. M. Deng, *Chemosphere*, **280**, 130626 (2021).
58. X. L. Yang, X. Y. Xie, S. Q. Li, W. X. Zhang, X. D. Zhang, H. X. Chai and Y. M. Huang, *J. Hazard. Mater*., **419**, 126360 (2021).
59. Y. W. Zhong, K. Shih, Z. H. Diao, G. Song, M. H. Su, L. A. Hou, D. Y. Chen and L. J. Kong, *Chem. Eng. J*., **417**, 129225 (2021).
60. J. B. Zhou, W. Liu and W. Q. Cai, *Sci. Total Environ*., **696**, 133962 (2019).
61. J. Y. Liu, Z. L. Li, M. Wang, C. Y. Jin, J. Kang, Y. W. Tang and S. Y. Li, *Sep. Purif. Technol*., **274**, 118666 (2021).
62. Q. Y. Zhang, X. Q. Sun, Y. Dang, J. J. Zhu, Y. Zhao, X. X. Xu and Y. Z. Zhou, *J. Hazard. Mater*., **424**, 127651 (2022).

# Supporting Information

# Synergistic and sustainable activation of peroxymonosulfate by nanoscale MWCNTs-$CuFe_2O_4$ as a magnetic heterogeneous catalyst for the efficient removal of levofloxacin

**Jing Zhao and Pengfei Xiao**†

College of Forestry, Northeast Forestry University, Harbin 150040, China
(*Received 11 August 2022 • Revised 4 October 2022 • Accepted 1 November 2022*)

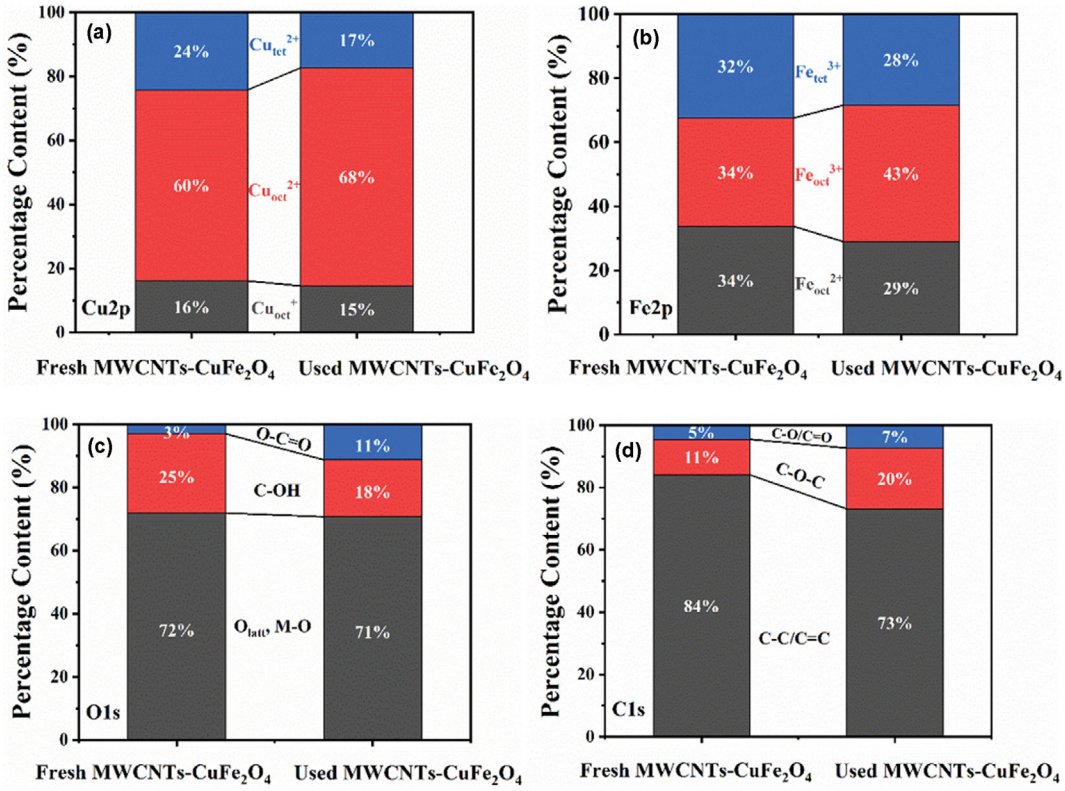


**Fig. S1. The contents of different Cu ions (a); different Fe 2p (b); containing oxygen bonds (c); and containing carbon bands (d) of fresh and used MWCNTs-$CuFe_2O_4$ (1 : 3).**

**Table S1. Removal kinetic constants of LEV in MWCNTs-$CuFe_2O_4$ (1 : 3, 1 : 5, 1 : 10, 1 : 20)/PMS systems**

| Catalyst | First-order kinetic | | | Second-order kinetic | | |
|---|---|---|---|---|---|---|
| | Rate equation | $k_{obs}$/$min^{-1}$ | $R^2$ | Rate equation | $k_{obs}$/$min^{-1}$ | $R^2$ |
| MWCNTs-$CuFe_2O_4$ (1 : 3) | $-\ln(C/C_0)=0.0565t+0.6072$ | 0.0565 | 0.7455 | $1/C-1/C_0=0.1556t+0.75$ | 0.1556 | 0.9125 |
| MWCNTs-$CuFe_2O_4$ (1 : 5) | $-\ln(C/C_0)=0.0557t+0.5085$ | 0.0557 | 0.7922 | $1/C-1/C_0=0.143t+0.5312$ | 0.143 | 0.9331 |
| MWCNTs-$CuFe_2O_4$ (1 : 10) | $-\ln(C/C_0)=0.0498t+0.4134$ | 0.0498 | 0.8165 | $1/C-1/C_0=0.1081t+0.3859$ | 0.1081 | 0.9357 |
| MWCNTs-$CuFe_2O_4$ (1 : 20) | $-\ln(C/C_0)=0.044t+0.1924$ | 0.044 | 0.9414 | $1/C-1/C_0=0.0745t+0.0557$ | 0.0745 | 0.9955 |

**Table S2. The degradation intermediate of LEV**

| Compound | Molecular structure | m/z value | Compound | Molecular structure | m/z value |
|---|---|---|---|---|---|
| P1 | 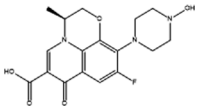 | 364 | P12 | 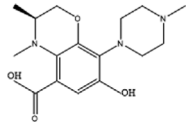 | 322 |
| P2 | 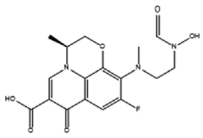 | 365 | P13 | 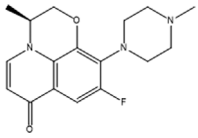 | 318 |
| P3 | 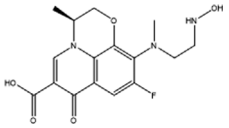 | 337 | P14 | 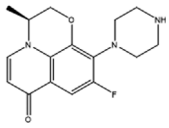 | 304 |
| P4 | 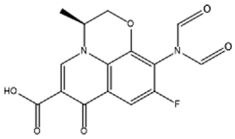 | 334 | P15 | 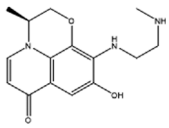 | 290 |
| P5 | 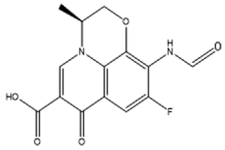 | 307 | P16 | 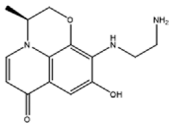 | 276 |
| P6 | 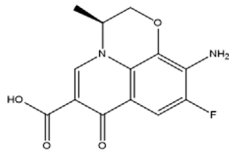 | 281 | P17 | 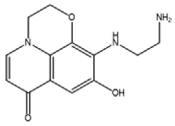 | 262 |
| P7 | 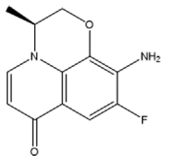 | 237 | P18 | 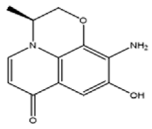 | 233 |
| P8 | 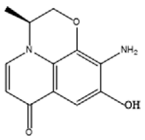 | 235 | P19 | 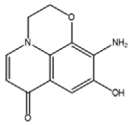 | 219 |
| P9 | 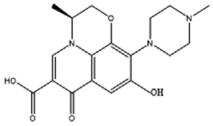 | 360 | P20 | 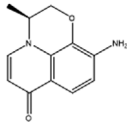 | 217 |
| P10 | 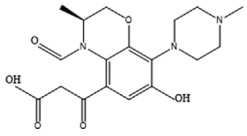 | 364 | P21 | 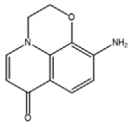 | 203 |
| P11 | 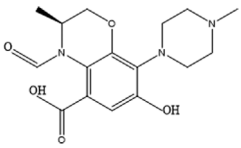 | 336 | | | |